



HAL
open science

Nanophononics in the GHz-THz range

Norberto Daniel N. D. Lanzillotti Kimura

► **To cite this version:**

Norberto Daniel N. D. Lanzillotti Kimura. Nanophononics in the GHz-THz range. Optics [physics.optics]. Université Paris-Saclay, 2021. ⟨tel-03631751⟩

HAL Id: tel-03631751

<https://hal.science/tel-03631751v1>

Submitted on 5 Apr 2022

HAL is a multi-disciplinary open access archive for the deposit and dissemination of scientific research documents, whether they are published or not. The documents may come from teaching and research institutions in France or abroad, or from public or private research centers.

L'archive ouverte pluridisciplinaire **HAL**, est destinée au dépôt et à la diffusion de documents scientifiques de niveau recherche, publiés ou non, émanant des établissements d'enseignement et de recherche français ou étrangers, des laboratoires publics ou privés.



HAL Authorization

Habilitation à Diriger des Recherches de l'Université Paris-Saclay

Nanophononics in the GHz-THz range

Dr. Norberto Daniel LANZILLOTTI KIMURA

Defense date: March 17th, 2021

Members of the jury

Prof. Hatice ALTUG

Ecole Polytechnique Fédérale de Lausanne, Switzerland

Prof. Markus ASPELMEYER

Universität Wien, Austria

Prof. Alexander BALANDIN

University of California at Riverside, USA

Prof. Vitalyi GUSEV

Université Le Mans, France

Prof. Lukas NOVOTNY

Swiss Federal Institute of Technology in Zurich, Switzerland

Prof. Odile STÉPHAN

Université Paris-Saclay, France

Prof. Eli YABLONOVITCH

University of California at Berkeley, USA

Chapter 1	Motivation	1
Chapter 2	Fundamentals of one-dimensional nanophononics.....	5
2.1	Simple nanoacoustic devices: mirrors and cavities.....	5
2.2	Experimental techniques	7
2.3	Discussion and conclusions.....	10
Chapter 3	Nanophononics as a simulation platform for solid-state physics.....	13
3.1	Mimicking the tight binding and nearly free electron models.....	13
3.2	Bloch oscillations of acoustic phonons	14
3.3	Effective potentials for acoustic phonons	15
3.4	Band inversion and topological interface modes.....	16
3.5	Discussion and conclusions.....	19
Chapter 4	Opto-phononic colocalization in GaAs/AlAs multilayers.....	21
4.1	GaAs/AlAs heterostructures as a platform for optophononics.....	21
4.2	Fabry-Perot resonators for light and sound.....	23
4.3	Optophononic topological modes	24
4.4	Anderson localization in perturbed superlattices	25
4.5	Discussion and conclusions.....	26
Chapter 5	Optophononic micropillars and acousto-plasmonic metasurfaces.....	29
5.1	Semiconductor micropillars as optophononic resonators	29
5.2	Brillouin scattering in nested micropillar resonators	30
5.3	Coherent phonon generation in optophononic micropillars	31
5.4	Towards fiber-integrated nanophononics	32
5.5	Polarization-controlled acousto-plasmonic metasurfaces.....	33
5.6	Acousto-plasmonic interferences	36
5.7	Discussion and conclusions.....	38
Chapter 6	Research perspectives	41
6.1	Integrated phonon networks: confinement and propagation	41
6.2	Reconfigurable optophononic devices	42
6.3	Quantum nanoacoustics.....	44
Bibliography	47
Acknowledgments	54

Chapter 1

Motivation

In classical mechanics, a phonon designates a normal vibrational mode, and it is naturally related to the concept of acoustic waves. Likewise, a phonon is the quantum mechanical description of an elementary vibrational motion in which a lattice of atoms or molecules uniformly oscillates at a single frequency. Every physical property of a solid-state system determined by the position of the atoms can be strongly affected by the presence of phonons. Acoustic phonons are usually seen as a primary source of unwanted effects in electronics, optoelectronics, and quantum technologies based on solid-state platforms. This work presents a series of nanodevices where *acoustic phonons* constitute, instead, a central resource to study novel physical phenomena. By controlling the acoustic phonons and their interactions with other excitations, a new degree of freedom appears in the design of solid-state devices.

Recent advances in phonon engineering have shown that it is possible to control the phonon dynamics and interactions in a wide range of systems and materials.¹⁻⁶ Exploiting the interactions of phonons with other excitations requires the full engineering of the phononic landscape in nanostructured systems, i.e., the local density of states and the confinement properties through phononic resonances.^{2,7} The flourishing activity in nanomechanics, cavity optomechanics,⁸ and electromechanics is based on novel architectures to confine phonons; we can cite a few examples: microdisks,^{9,10} microtoroids, photonic/phononic crystals^{11,12}, "zipper" resonators,^{13,14} liquid resonators,^{15,16} among many others^{4,17}. Stunning acoustic phenomena have been recently reported, including the coupling between a superconducting qubit and a vibrational mode,¹⁸ the hybridization of mechanical resonators and electrical microwave cavities,¹⁹ the use of mechanics to interface microwaves and optical photons,²⁰ the coupling of propagating surface acoustic waves (SAWs) to a superconducting qubit of the transmon type²¹ and the demonstration of an acoustic Hong-Ou-Mandel experiment.²² Most of the resonators used in these demonstrations rely entirely on the quality of top-down microfabrication methods, imposing limitations on the smallest feature in the system and thus in the highest achievable frequency. Consequently, these and other appealing results were obtained mainly in the low-frequency regimes, from kHz to hundreds of MHz, reaching a few GHz in some particular cases.

In the early stages, the control of acoustic phonons was strongly inspired by developments in nanophotonics,²³⁻²⁶ in particular by photonic crystals. Nanophononics^{1,27,28} evolved as a new field of physics proposing the engineering of phononic fields at the nanoscale and ultrahigh frequencies. Some of the milestones in ultrahigh-frequency nanophononics include the demonstration of an acoustic nanocavity²⁹⁻³¹, the report of phonon lasing effects³²⁻³⁴, the use of piezoelectric transducers in the sub-THz regime³⁵, a laser mode feeding by 'shaking QDs',³⁶ the study of phonon dynamics in nanoparticles³⁷ and complex systems³⁸, the subwavelength acoustic imaging using acousto-plasmonics,^{39,40} and the magneto-acousto-plasmonic⁴¹ structures, and the study of phoXonic structures^{31,42-45} just to name a few.

Several characteristics make nanophononics a promising research field: i) taking advantage of the interaction with optical systems, acoustic phonons could be used to develop ultra-high frequency acousto-optic modulators; ii) the small thermal occupation numbers associated to ultrahigh frequency acoustic phonons imply that for resonators working in the tens of GHz, it is feasible to reach the quantum regime with standard cryogenic techniques, enabling quantum nanoacoustics; iii) through their interactions with other excitations, acoustic phonons can be used to interface different (quantum) platforms; iv) the short wavelength can be directly associated with higher resolution in the development of novel nanoscopies; v) acoustic phonons are one of the main heat carriers, and nanophononics could propose innovative thermal management schemes;⁴⁶⁻⁴⁸ and vi) the long mean free path, short wavelength, and the possibility of transducing the signals into other fields make nanoacoustics a perfect platform to study wave-dynamics phenomena that are difficult or impossible to investigate in electronic or optical systems. In a nutshell,

nanophononics is a versatile platform to simulate wave phenomena and is relevant for developing novel thermal management strategies, non-destructive testing tools, optomechanical platforms, and quantum technologies.

While the objectives and potential are clear, the path is still uncharted. Many fundamental questions in nanophononics remain unanswered: how can acoustic phonons be efficiently generated and detected? How can we confine them and control their propagation? What is their mean free path, and how is it affected in nanostructures? How can the interactions with other excitations be engineered and controlled? Can phonons be used as nanoproboscopes? Can phonons carry information? How can we use acoustic phonons to study the dynamics of other solid-state phenomena? All these questions can be grouped around three challenges: master the transduction mechanisms beyond the few-GHz range, manipulate the local acoustic density of states and confinement properties and control the phonon dynamics and transport.

My activities in this field started in 2004, in the Laboratorio de Propiedades Opticas of the Centro Atomico Bariloche, in Argentine. During my MEng, under the direction of Prof. Alejandro Fainstein, we developed the first series of complex devices, including mirrors and cavities. These devices have constituted the building blocks to explore novel physical phenomena during my career. As part of a cotutelle program, I carried out my Ph.D. between the Instituto Balseiro, Universidad Nacional de Cuyo (Argentine), and the Institut des NanoSciences de Paris, Université Paris 6 (France), under the direction of Prof. Alejandro Fainstein and Prof. Bernard Perrin. During this time, I investigated the phonon dynamics in nanometric multilayered structures, work that I continued as a researcher in Argentine until October 2010.

In 2010, I joined the group of Prof. Xiang Zhang at the University of California at Berkeley. During my postdoctoral research, I theoretically proposed and experimentally demonstrated acousto-plasmonic devices, addressing the use of antennas to detect complex phonon modes' spatial properties through the interplay between plasmons and phonons. I also participated in other research activities related to general plasmonics, optical metamaterials, and the development of optoelectronic devices.

From 2013 to 2015, I joined the groups of Prof. Pascale Senellart at Laboratoire de Photonique et de Nanostructures (LPN) and Prof. Ivan Favero at the Laboratoire Matériaux et Phénomènes Quantiques (MPQ) in France. We obtained the first results on the characterization of micropillar optophononic resonators, I was trained in the physics and fabrication of single-photon sources, and we acquired the first spectra of topological nanophononic interface modes.

Since 2015, I work as a tenured researcher of the CNRS at the Centre de Nanoscience et de Nanotechnologies (C2N) in Palaiseau, France, developing a full research line in nanomechanics and nanophononics. In 2016 I was awarded an ERC Starting Grant for a project on nanophononics, which constitutes the backbone of my research.

This manuscript condensates my contributions to the field of nanophononics. I organized it around challenges, highlighting some relevant results obtained during my career and showing their relevance and implications for the research field. In each chapter, I present the conclusions and outline some future work perspectives following the main results and reference some of the articles related to the main contributions presented in the chapter.

Chapter 2 is devoted to briefly introducing the fundamentals of nanophononics in heterostructures, presenting the experimental techniques, and giving the reader the necessary references to address the content of the following chapters. The simplest acoustic phonon devices are presented in this chapter: mirrors and Fabry-Perot acoustic cavities based on nanophononic crystals. The phonon dynamics in these devices is studied in the time domain by pump-probe coherent phonon generation and high-resolution Brillouin scattering in the spectral domain. The nanophononic devices are optimized to work in the 10-1000 GHz range.

In Chapter 3, I address the band engineering concept to control the acoustic phonon dynamics. These ideas allow us to present two strategies following the nearly-free-electron and the tight-binding models to

simulate and mimic a variety of Hamiltonians in solid-state physics. In particular, I introduce the Bloch oscillations of acoustic phonons by implementing linear potentials. Extending the electronic and acoustic bands analogy allows us to propose topological acoustic systems at the nanoscale.

Acoustic phonons in the hundreds of GHz present wavelengths that are at least one order of magnitude shorter than visible photons. In this frequency range, nanophononics meets classical Raman and Brillouin spectroscopies. When considering audible acoustic waves, or ultrasound, the opposite is true: the optical wavelength is much shorter than the acoustic wavelength: this is the domain of classical photothermal and photoacoustic effects. But, what happens when the wavelength of the light matches the wavelength of the sound? And more importantly, how can we engineer these conditions in real-life samples? Chapter 4 explores resonators based on GaAs/AlAs that can simultaneously confine near-infrared photons and acoustic phonons of around 20 GHz. We analyze three cases: i) Fabry-Perot resonators for light and sound; ii) optophononic topological modes, and iii) Anderson localization in perturbed periodic superlattices.

The devices presented in the previous chapters are based on planar structures, where the acoustic density of states presents variations in one direction. For most applications, however, it is necessary to reach full control of the three-dimensional density of states. Chapter 5 presents two kinds of opto-phononic devices that rely on the confinement of light and sound in the three dimensions of space: semiconductor micropillar cavities and acousto-plasmonic metasurfaces.

Chapter 6 discusses the main ideas of my scientific project's core in the upcoming years, organized around three main open challenges in nanophononics: transport and confinement, the quantum regime, and tunability.

Chapter 2

Fundamentals of one-dimensional nanophononics

Phononic crystals, the acoustic equivalent of photonic crystals,^{23,24} have potential applications in studying fundamental wave phenomena, non-destructive characterization, quantum technologies, and thermal transport. Recently, phononics and, more specifically, nanophononics became a very active field of research. There are, however, early reports such as the work of Narayanamurti et al. in 1979,⁴⁹ where the authors investigate the propagation of high-frequency acoustic phonons through a superlattice. Usually inspired by photonics concepts, a plethora of nanophononic devices based on phononic Bragg reflectors were reported over the last decades: mirrors, cavities,^{2,7} and filters,^{28,50,51} among others.

Two simultaneous developments accelerated the progress of nanophononics. On the one hand, the fast advancements in growth and fabrication techniques, mostly motivated by the nanoelectronics and optoelectronics communities, enable the generation of acoustic structures on the nm scale; on the other hand, the proposal of novel experimental techniques based on pump-probe schemes to study acoustic-phonon dynamics.^{52,53}

This chapter briefly introduces one-dimensional mirrors and cavities, the simplest nanophononic devices, and two widely used experimental techniques to characterize them, pump-probe coherent phonon generation and spontaneous Brillouin scattering.

2.1 Simple nanoacoustic devices: mirrors and cavities

In general, the dispersion relation of acoustic phonons in a bulk material is approximately linear. A superlattice (SL) of two materials with contrasting acoustic impedances results in a folding of the acoustic-phonon dispersion relation, with gaps appearing at the new Brillouin zone center and edge (see Figure 1). Finite-size SLs present high-reflectivity stopbands that are associated with the bandgaps of their periodic infinite counterparts.

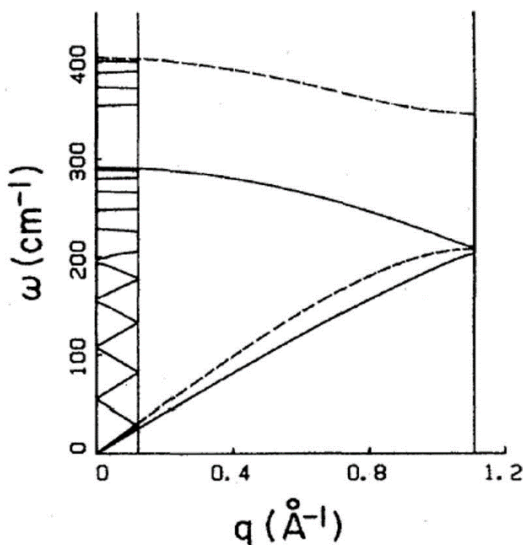


Figure 1: Phononic dispersion relations of GaAs and AlAs. A superlattice of made of the two materials induces a folding and the opening of minigaps at the Brillouin zone edge and center. Adapted from Ref. 57.

A periodic multilayer constitutes one of the simplest semiconductor nanophononic devices: a mirror. Similar to the electronic and optical analogs, these one-dimensional phononic crystals can be engineered and optimized. The relevant engineering parameters are the speed of sound and the acoustic impedance of the used materials. The acoustic impedance is defined as the product of the speed of sound times the mass density.

By looking at the wave equations describing the propagation of acoustic and electromagnetic waves through an interface, and the corresponding boundary conditions, the contrast in the indices of refraction can be related to the contrast of the acoustic impedances in the materials. The sound speed determines the acoustic wavelength for a given frequency, while the speed of light determines the optical wavelength.⁵⁴⁻⁵⁶

Phonon mirrors are usually optimized for a single polarization and a single propagation direction. Unless the

contrary is stated, in this work, we address exclusively longitudinal acoustic phonons propagating in the direction where the modulation of the elastic properties is present.

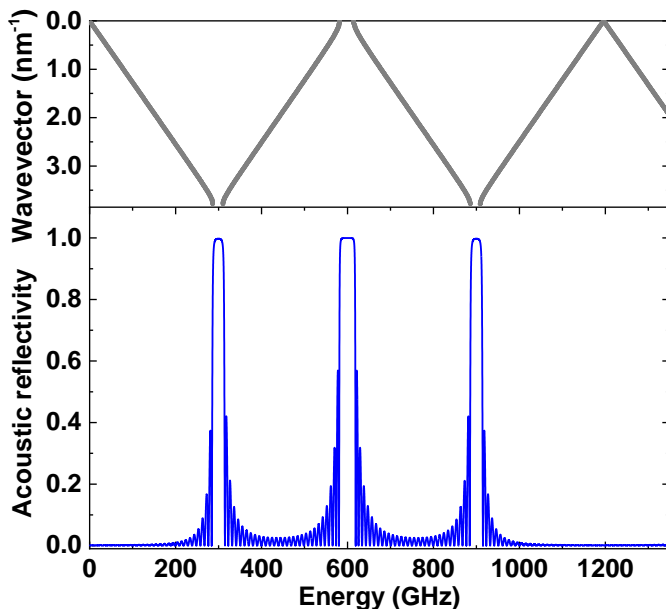


Figure 2: Phononic Bragg reflector made of a $(\lambda/4, 3\lambda/4)_{20}$ array of (GaAs/AlAs) for a frequency of 600 GHz. Top panel: associated dispersion relation of an infinite superlattice. Bottom panel: calculated acoustic reflectivity considering an infinite GaAs surrounding medium.

optical semiconductor DBR made of GaAs/AlAs bilayers is optimized to work at 900 nm, the second-order minigap would fall in a region of strong absorption. In the case of acoustic stopbands, the elastic properties remain roughly constant over large energy bands.

The thickness ratio $(\lambda/4, 3\lambda/4)$ maximizes the second minigap, i.e., the first minigap at the Brillouin zone center. Figure 3 shows the reflectivity as a function of frequency and thickness ratio for a DBR with a first minigap at the Brillouin zone center at 20 GHz. We observe that the first minigap reaches a maximum width at $(\lambda/2, \lambda/2)$, while the second minigap does it at $(3\lambda/4, \lambda/4)$ and $(\lambda/4, 3\lambda/4)$. The n^{th} -order minigap closes $n+1$ times when spanning the thickness ratio from 0 to 1. The contrast in the acoustic impedances, thickness ratio, and the number of SL periods determine the reflectivity of a DBR.^{57,58}

Although periodicity is usually associated with the constructive and destructive interferences generating the stopbands, it is not a strong requirement. Starting from perfectly periodic structures, we introduced tailored perturbations to achieve complex functionalities. For example, complex response devices like broadband reflectors, color and notch filters, and special cavities can be designed and fabricated using optimization algorithms that break the periodicity by either changing the thickness or the composition of the layers in a SL.^{28,50,51,55,59}

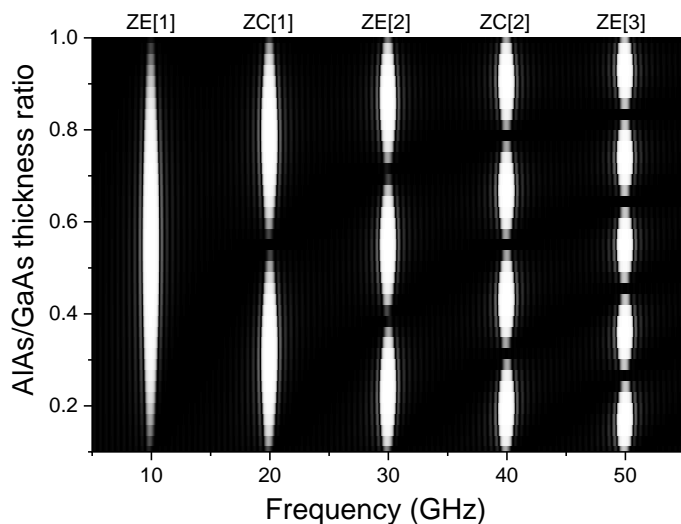


Figure 3: Intensity map showing the acoustic reflectivity of a $(\text{GaAs}/\text{AlAs})_{20}$ SL as a function of the frequency and thickness ratio in the unit cell. Notice how the minigaps open and close as the thickness ratio varies. ZE and ZC stand for Brillouin zone edge and center, respectively.

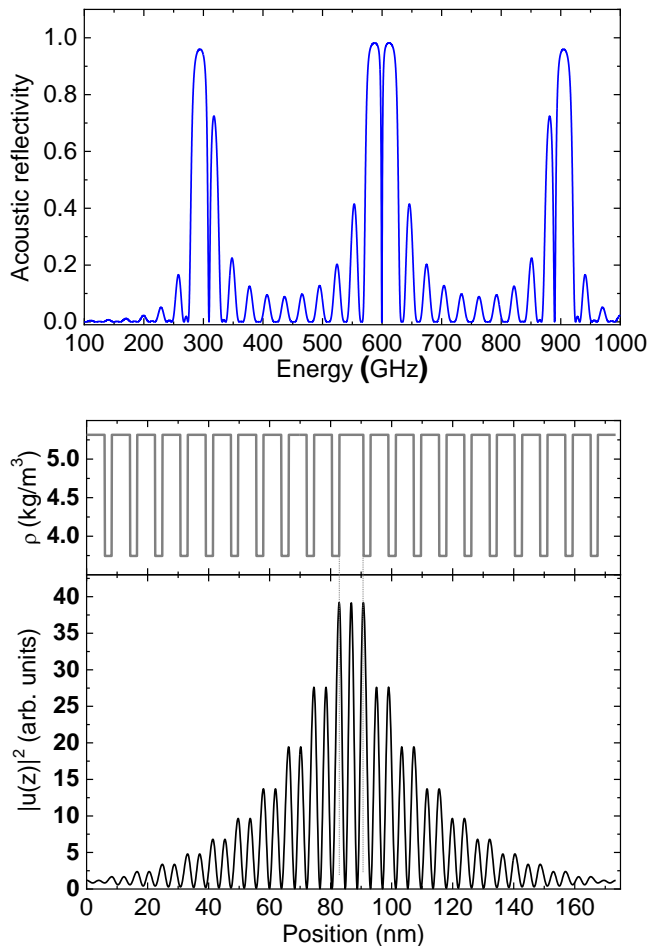


Figure 4: Acoustic nanocavity made of two DBRs $(\lambda/4, 3\lambda/4)_{10}$ and a λ GaAs spacer. Top: calculated acoustic reflectivity. Bottom: displacement profile corresponding to the 600 GHz confined mode showing an enhancement of the field at the spacer position.

cavity spacers of an integer number of wavelengths result in Raman-inactive modes. An acoustic cavity working at 600 GHz, formed by two DBRs $(\lambda/4, 3\lambda/4)_{10}$ and a λ GaAs spacer has a total thickness of ~ 175 nm, and typical Q-factors reach values of 10^3 - 10^4 .^{12,63}

2.2 Experimental techniques

Beyond a few GHz, in addition to the limitations encountered in the fabrication of top-down nanomechanical resonators, there are no standard and efficient transducers that allow us to generate and detect acoustic vibrations. Thus, most of the experiments rely on optical techniques. This section discusses the experimental details of two flagship experiments in nanophononics: spontaneous Brillouin scattering^{64,65} and pump-probe coherent phonon generation and detection experiments.^{52,53} These techniques allow accessing the spectral and temporal characteristics of the studied devices. For the sake of simplicity, we do not discuss noise spectroscopy techniques and stimulated Brillouin scattering, usually used in optomechanics experiments and in fibered platforms.

2.2.1 Raman and Brillouin scattering

A simple Raman/Brillouin scattering experiment consists of the excitation of a sample using a continuous wave laser and analyzing the scattered light using a spectrometer. A small fraction of the incident light inelastically scatters. The difference in the energy between the incident and scattered light is directly related to the scattering media's excitation energy. When the considered excitations are acoustic (optical) phonons, the process is usually referred to as Brillouin (Raman) scattering. Figure 5 shows a scheme of the

The second simplest one-dimensional phononic device is an acoustic cavity (see Figure 4).^{2,7,12} It is the phononic equivalent of an optical Fabry-Perot resonator. In this nanoacoustic analog, we replace the metallic mirrors with two acoustic DBRs, and a GaAs crystalline layer forms the spacer. The system presents a resonance each time the spacer thickness matches an integer number of half-wavelengths, and the reflectivity of the DBRs determines the quality factor of the cavity.^{2,56}

Widely used in photonics, the semiconductor optical microcavities based on optical DBRs have shown many applications, being at the base of studies on nonlinearities, polaritonics, spectroscopy, and quantum devices.⁶⁰⁻⁶² The similarities between acoustic and optical systems imply that all the know-how developed in photonic systems could be easily mapped into nanophononics.⁵⁶

The acoustic reflectivity of the mirrors determines the quality factor of the resonator. The cavity mode's spectral position is mainly determined by the spacer's thickness, being the standard case an integer number of half-wavelengths. It is worth noting that due to symmetry reasons,

experimental setup. In this work, we focus our attention on the backscattering configuration, i.e., the scattered photons propagate in approximately the opposite direction of the incident laser.

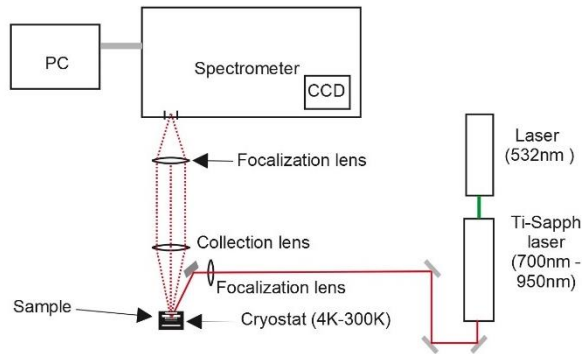


Figure 5: Schematics of a generic Brillouin scattering setup where a CW laser excites a sample located in a cryostat. The scattered light is collected and analyzed by a spectrometer.

achieved by exploiting the in-plane photon dispersion of the optical cavity mode. The wavenumber \mathbf{k} of the optical mode in the cavity can be decomposed as $\mathbf{k} = \mathbf{k}_z + \mathbf{k}_{//}$ where $\mathbf{k}_{//}$ is the in-plane component and \mathbf{k}_z is the normal component. The resonance is achieved for a given \mathbf{k}_z . The in-plane component $\mathbf{k}_{//}$ increases with the angle of incidence. Therefore, keeping \mathbf{k}_z constant and varying $\mathbf{k}_{//}$ implies a blue-shift of the optical cavity resonance when tuning the angle of incidence away from the surface normal. Both Stokes and anti-Stokes processes can be selectively enhanced by adequately choosing the incidence and collection angles. Under this condition, the excitation laser and the Brillouin scattered signal are coupled to the optical cavity mode.

In the top panel of Figure 6 we show the calculated acoustic reflectivity of an acoustic cavity optimized for 18 cm^{-1} . The lower panel presents the Raman scattering spectra measured on a hybrid optophononic sample measured under DOR conditions.⁶⁹ Usually, the samples consist of an acoustic structure acting as the spacer of an optical cavity. In this way, the signal is strongly amplified. The spectra were taken on different positions of a wafer grown with a gradient, so the optical cavity resonance is position-dependent. A clear, intense peak at $\sim 18 \text{ cm}^{-1}$ indicated CM corresponds to the confined acoustic phonons in an acoustic nanocavity.⁶⁹ The rest of the peaks in the spectra correspond to modes distributed over the DBRs. The spectrum highlighted in red corresponds to the particular DOR condition. Further details and examples of hybrid optophononic samples and the DOR condition can be found in refs.^{7,59,59,63,65,67,69-71}

One of the major experimental challenges is eliminating the stray light due to the low intensity of the involved signals and the intense laser's spectral proximity. Optical microcavities can be used to enhance the signals. Introduced by A. Fainstein in nanophononics, the idea behind the double optical resonance is to strongly enhance both the incoming (excitation) and the scattered (Raman/Brillouin) fields. To simultaneously achieve an incoming and outgoing resonance at slightly different wavelengths, it is possible to use the angular dispersion in planar optical microcavities.⁶⁵⁻⁶⁹

The double optical resonance (DOR) condition is achieved by exploiting the in-plane photon dispersion of the optical cavity mode. The wavenumber \mathbf{k} of the optical mode in the cavity can be decomposed as $\mathbf{k} = \mathbf{k}_z + \mathbf{k}_{//}$ where $\mathbf{k}_{//}$ is the in-plane component and \mathbf{k}_z is the normal component.

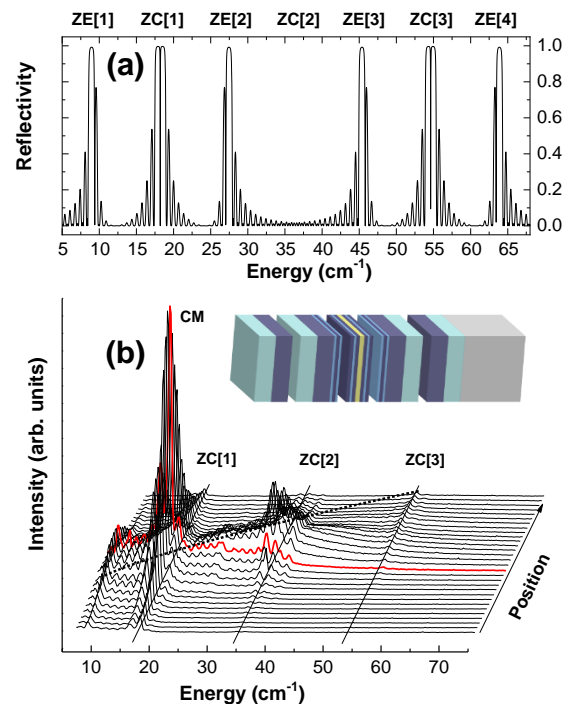


Figure 6: Top panel: calculated reflectivity of the acoustic nanocavity. Bottom panel: measured Raman-scattering spectra varying the spot position on the sample taken at room temperature with an incidence angle of $\sim 15^\circ$ and a laser wavelength of 815 nm. Continuous lines indicate the acoustic band-gap positions; the dotted line is a guide to the eyes for the optical mode spectral position. CM, ZC[2], and ZC[3] stand for cavity mode in the first minigap at the Brillouin zone center, and second and third folded acoustic phonons at the Brillouin zone center, respectively. The inset shows a schematics of the sample. Adapted from Ref. 69.

2.2.2 Coherent phonon generation and detection

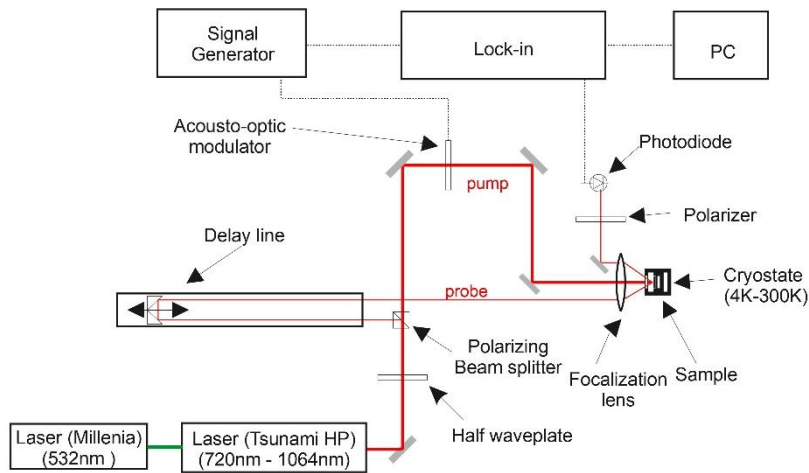


Figure 7: Schematics of a generic pump-probe coherent phonon generation setup.

Proposed initially by Thomsen et al.,^{52,53} the technique uses ultrafast laser pulses. A Titanium:Sapphire laser produces fs/ps pulses at an ~ 80 MHz repetition rate in a standard scheme. The laser beam is split in two (pump and probe) following different paths, as shown in Figure 7. The probe beam passes through a mechanical delay line to control the relative delay between pump and probe pulses. The pump beam goes through an acousto-optic modulator allowing synchronous detection using a lock-in amplifier.

Both beams are focused on the sample. The pump pulse impulsively generates coherent phonons with periods much longer than the pulse duration.⁷² These phonons modulate the optical properties of the sample with GHz frequencies. We use a cross-polarization scheme, and a photodetector measures the resulting changes in the delay-dependent reflectivity experienced by the probe pulse. A lock-in amplifier extracts differential reflectivity time traces like the ones shown in Figure 8. By Fourier transforming the time traces, the frequencies of the coherent acoustic phonons are recovered. In this case, the sample consists of an optimized DBR to work at frequencies slightly higher than 1 THz.

We can mention the different processes that participate in the coherent phonon generation: photothermal, deformation potential, and electrostriction. We can identify two main mechanisms for detecting coherent acoustic phonons: the displacement of the interfaces in the studied sample and the change in the materials' dielectric function.^{52,53,72,73} The choice of materials and structures thus becomes an integral part of the design of the experiments.

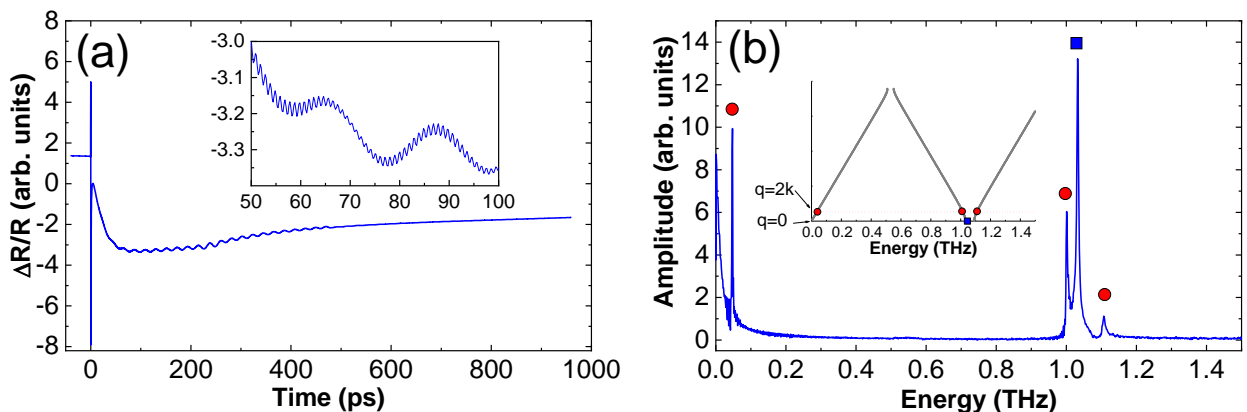


Figure 8: Pump-probe measurements on an acoustic superlattice ($\lambda/4$, $3\lambda/4$) made of (AlAs/GaAs). (a): Time trace of optical reflectivity measured on a superlattice. The inset shows a detailed view of the reflectivity oscillations induced by the coherent acoustic phonons. (b): Fourier transform of the reflectivity temporal evolution, after having removed the low frequency components. The red circles and blue rectangle indicate the peaks associated to mechanical modes verifying $q = 2k$, and $q = 0$, respectively. The inset shows the band diagram of the associated superlattice.

2.2.3 Beyond the standard techniques

Recently, we proposed a versatile Brillouin spectroscopy scheme to measure acoustic phonons in the 20-300 GHz frequency range without optical wavelength restriction, thereby overcoming the limitations of

existing optimized Raman and Brillouin spectrometers.⁷⁴ The experiments were performed on semiconductor optophononic planar cavities with typical quality factors of ~ 2000 , where the mode of the optical cavity enhances the Brillouin scattering signal. We proposed combining angular and spectral filtering techniques to observe the confined acoustic modes in the Brillouin spectrum with sufficiently high spectral resolution and contrast. The angular filtering is implemented with a single-mode fiber to efficiently filter out stray light from the laser and increase the signal-to-background ratio. The additional spectral filtering is implemented through a tandem of an etalon and double Raman spectrometer. This combination has enabled us to observe the low-frequency acoustic modes of a cavity at 20 GHz with a simple etalon, otherwise concealed in the excitation laser background.⁷⁴

Concerning the efficient generation of coherent acoustic phonons, it relies on an efficient coupling of the pump field into the system, while the sensitive detection of phonons requires an efficient coupling of the probe to the optical mode undergoing a phonon-induced modulation. The main practical challenges for implementing this technique are 1) stability, 2) reproducibility, and 3) high power densities limiting the range of compatible samples. We recently integrated fibered systems to eliminate any optical alignment on the sample, thus simultaneously solving the three aforementioned main problems.⁷⁵ This implementation is discussed in Chapter 5.

2.3 Discussion and conclusions

In this chapter, we presented two simple one-dimensional acoustic devices at the nanoscale: mirrors and cavities. These devices are based on multilayers forming one-dimensional phononic crystals. As such, the wavelength of the considered phonons determines the characteristic length. Traditionally, the devices' functionality arises from a periodicity in the multilayer, as in distributed Bragg reflectors. By combining two DBRs separated by a spacer, it is possible to construct an acoustic cavity with resonances similar to a Fabry-Perot resonator. The characteristic thickness determines the operating frequency of the device. In this way, the multilayers allow reaching two different acousto-optic regimes. When considering frequencies higher than 100 GHz, the multilayer acts as an effective medium for light, and a large number of layers can be grown using MBE.^{28,50,55,56,76} This is particularly relevant when studying samples like the ones proposed in Chapter 3. When considering phonons of ~ 20 GHz, the wavelength of the acoustic phonons matches the wavelength of NIR photons. This particular case is addressed in Chapter 4 for GaAs/AIAs heterostructures.

The multilayers are far from their limits in terms of applications. For instance, using the discrete modes of acoustic resonators, they can constitute the building block of complex structures able to simulate solid-state phenomena. This strategy is briefly presented in Chapter 3. By etching planar wafers into micropillars' shapes, it is possible to induce three-dimensional confinement, thus engineering the local 3D acoustic (and optical) density of states, and it constitutes part of the subjects presented in Chapter 5.

The presented GaAs/AIAs devices are compatible with quantum dots and quantum wells, giving access to novel physical phenomena where the engineering of the acoustic degree of freedom appears as a new knob to design optical, optoelectronic, and quantum devices. Some of these ideas are presented in Chapter 6.

Contributions related to this chapter

Since my Ph.D. I contributed to the conception of samples combining optical cavities and acoustic cavities working in the 20 GHz – 1 THz. Over the last years, my team developed and implemented novel experimental protocols and techniques that allowed us to unveil acoustic phonon dynamics and control the light-matter interactions in multilayered structures.

- A. Subterahertz Phonon Dynamics in Acoustic Nanocavities
Huynh, [N. D. Lanzillotti-Kimura](#), B. Jusserand, B. Perrin, A. Fainstein, M. F. Pascual-Winter, E. Peronne, and A. Lemaître
Phys. Rev. Lett. **97**, 115502 (2006).
- B. Coherent Generation of Acoustic Phonons in an Optical Microcavity
[N. D. Lanzillotti-Kimura](#), A. Fainstein, A. Huynh, B. Perrin, B. Jusserand, A. Miard, and A. Lemaître
Phys. Rev. Lett. **99**, 217405 (2007).
- C. Resonant Raman Scattering of Nanocavity-Confined Acoustic Phonons
[N. D. Lanzillotti-Kimura](#), A. Fainstein, B. Jusserand, and A. Lemaître
Phys. Rev. B **79**, 035404 (2009).
- D. Nanophononic Thin-Film Filters and Mirrors Studied by Picosecond Ultrasonics
[N. D. Lanzillotti-Kimura](#), B. Perrin, A. Fainstein, B. Jusserand, and A. Lemaître
Appl. Phys. Lett. **96**, 053101 (2010).
- E. Enhancement and Inhibition of Coherent Phonon Emission of a Ni Film in a BaTiO₃ / SrTiO₃ Cavity
[N. D. Lanzillotti-Kimura](#), A. Fainstein, B. Perrin, B. Jusserand, A. Soukiassian, X. X. Xi, and D. G. Schlom
Phys. Rev. Lett. **104**, (2010).
- F. Coherent Control of Sub-Terahertz Confined Acoustic Nanowaves: Theory and Experiments
[N. D. Lanzillotti-Kimura](#), A. Fainstein, A. Lemaitre, B. Jusserand, and B. Perrin
Phys. Rev. B **84**, 115453 (2011).
- G. Mesoporous Thin Films for Acoustic Devices in the Gigahertz Range
N. L. Abdala, M. Esmann, M. C. Fuertes, P. C. Angelomé, O. Ortiz, A. Bruchhausen, H. Pastoriza, B. Perrin, G. J. A. Soler-Illia, and [N. D. Lanzillotti-Kimura](#)
J. Phys. Chem. C **124**, 17165 (2020).
- H. Fiber-Based Angular Filtering for High-Resolution Brillouin Spectroscopy in the 20-300 GHz Frequency Range
A. Rodriguez, Priya, O. Ortiz, P. Senellart, C. Gomez-Carbonell, A. Lemaître, M. Esmann, and [N. D. Lanzillotti-Kimura](#)
Optics Express **29**, 2637, (2021).

Chapter 3

Nanophononics as a simulation platform for solid-state physics

Nanophononic structures could provide the means to mimic and study solid-state physics phenomena challenging or impossible in optical and electronic platforms. A wave equation describes the propagation of acoustic waves in solid media, where the relevant parameters are the material mass density and sound velocity. The boundary conditions establish the connection between displacement and strain between two different materials. By mapping the wave equations from quantum mechanics and electromagnetism, concepts previously applied to electrons and photons can be directly extended to phononic structures. For frequencies in the GHz-THz range, the phonon wavelength is only a few nanometers, and thus the total sample thickness results much thinner than the optical equivalents. The required interface layer quality is achievable with molecular beam epitaxy technology and other standard growing techniques. Acoustic-phonon mean-free paths are long compared to the structure size (typically below one micron), and thus dephasing is not an issue as in the case of electronic crystals. Equally important, the available picosecond ultrasonic techniques give direct access to the waves' amplitude and phase information.

The acoustic phonons lack charge, and thus accelerating them, or equivalently changing their kinetic energy results, at the very least, challenging. This chapter explores two approaches to simulate the effects of effective potentials for acoustic phonons. By performing an engineering of the band structures in SLs and coupled-cavity systems, it is possible to slow down a wavepacket, change the sign of propagation, and manipulate different mode symmetries. The latter allows us to study the topological properties of nanoacoustic superlattices and implement topological interface modes.

3.1 Mimicking the tight binding and nearly free electron models

Effective potentials for acoustic phonons can be implemented based on the engineering of band structures to modify the group velocity over a multilayered structure. The bands can arise from periodic superlattices⁶⁴ or coupled identical acoustic nanocavities^{55,56}, i.e., the acoustic equivalent of coupled-resonator optical waveguides (CROWs)⁷⁷⁻⁷⁹.

Acoustic nanocavities provide localized acoustic states similar to the confined electronic levels in atoms and quantum wells. The cavities can couple through DBRs, leading to the formation of phononic minibands, mimicking the tight-binding model.⁵⁶ The minibands' width and the effective sound velocity in these structures can be engineered by the appropriate choice of the acoustic DBRs. The reflectivity of the mirror between two spacers determines the hopping probability from adjacent cavities, while the resonant

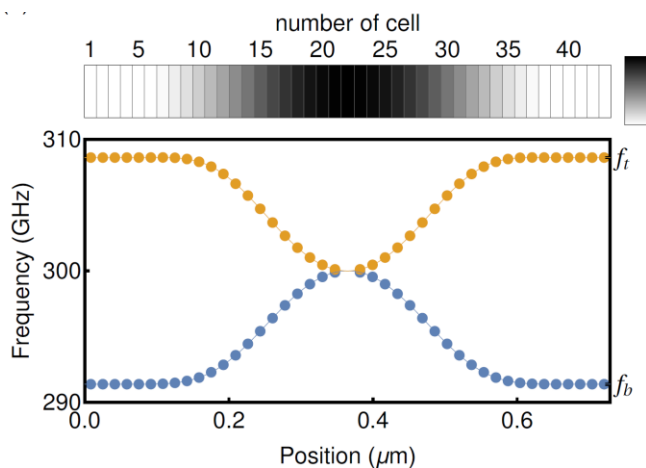


Figure 9: Top: Schematic of an adiabatic perturbation induced in a periodic structure of 43 unit cells. The grayscale indicates the ratio of AlAs/GaAs for each cell. Its modulation follows a \cos^2 shape between cells 6 and 38. In the extremes of the structure, the ratio is $(\lambda/4, 3\lambda/4)$ while at the center it reaches $(\lambda/2, \lambda/2)$. Layer thicknesses for cells with at the extremes are 4.72 nm and 11.95 nm for AlAs and GaAs layers, respectively. Bottom: Local acoustic band structure representing the minigap edges for each cell as a function of position. Each vertically aligned pair of dots corresponds to the minigap edges associated with each cell. Adapted from Ref. 55.

frequency of the cavities can easily tune the energy of the acoustic bands. The implementations based on this concept benefit from the versatility and simplicity of the structure. A spatial-dependent energy gradient, equivalent to the electric field for electrons, can be achieved, e.g., by varying the layer composition or thickness. Following this approach, we can map previously explored optical phenomena^{25,26,80} into a nanoacoustic platform. The dynamics of phonons can thus be tailored by coupling acoustic cavities in double^{56,81,82} and multiple cavity devices.^{56,76,81,83}

An alternative strategy to implement effective phonon potentials consists of directly performing a band engineering using a SL, simulating the nearly free electron model. In this case, the two relevant parameters are the energy and bandgap widths, which can be locally controlled by the SL period and relative thickness between the two materials forming the unit cell. In Figure 9, we show an adiabatic cavity example, where the SL ($\lambda/4$, $3\lambda/4$) with a maximally open second minigap at 300 GHz is adiabatically deformed at the center to reach ($\lambda/2$, $\lambda/2$) unit cell, closing the minigap. The top panel represents the layer thickness through the structure, where white layers represent a ($\lambda/4$, $3\lambda/4$) unit cell, while dark layers a ($\lambda/2$, $\lambda/2$). This structure presents two confined states at ~ 295 GHz and ~ 305 GHz and can be compared to an electronic potential well.⁵⁵ The implementations based on this concept benefit from smoother structure gradients, and in general, much thinner samples, allowing the realization of more complex potentials.

3.2 Bloch oscillations of acoustic phonons

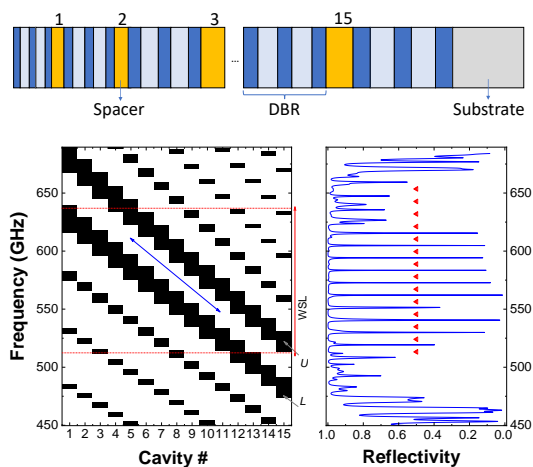


Figure 10: Top: Schematic of the coupled nanocavities nanostructure. Bottom left: Phonon band structure. The central region (indicated with a double arrow) limited by the thicker black forbidden bands corresponds to the cavity mode band. L, U, and WSL indicate the lower and upper minigaps, and the acoustic WSL region. Bottom right: Calculated acoustic reflectivity. Red triangles indicate the resonance energies of the isolated nanocavities. Adapted from Ref. 76

in principle, easier to observe.⁸³

To demonstrate the Bloch oscillations of acoustic phonons, we designed a structure formed by concatenated cavities (following the tight-binding model) where the energy of the i^{th} cavity must differ from that of the $(i-1)^{\text{th}}$ in a constant value. Such a linear dependence of the phonon cavity-mode energy with the position, analogous to an electric field for electrons, can be obtained by tuning the cavity widths. We thus consider a multilayer superstructure where each unit cell consists of an acoustic-phonon mirror made by $(n+1/2)$ periods [$\lambda/4$ (AlAs) / $3\lambda/4$ (GaAs)] in the examples discussed here, followed by a λ (GaAs) cavity. This unit cell is repeated N_c times with layer thicknesses increasing from the surface to the substrate to have a linear decrease of cavity-mode energy by steps Δ . We show the associated band structure and calculated reflectivity in the lower panels of Figure 10. Note that the energy of the individual cavities (indicated with red triangles) does not match the eigenenergies of the full superstructure (evidenced by the transmission lines in the reflectivity spectrum).

Electronic Bloch oscillations, i.e., oscillations of an electron induced by a constant electric field in the presence of a periodic potential, are a beautiful and clear example of quantum effects in solids.^{84,85} When an electric field is applied to a charged particle in a crystal, its wave vector increases with time. After that, Bragg interference leads to a velocity reduction and a sign change at the band edge. Notwithstanding its simplicity, for many years, the issue was controversial, and only quite recently, the existence of electronic Bloch oscillations has been experimentally established. In normal crystals, the large Brillouin zone and electron relaxation lead to an overdamped behavior characterized by Ohm's law. Instead, electronic Bloch oscillations are observable in semiconductor superlattices due to the Brillouin zone reduction.^{86,87} Acoustic phonons have long mean free paths compared with the size of acoustic resonators, and thus Bloch oscillations are,

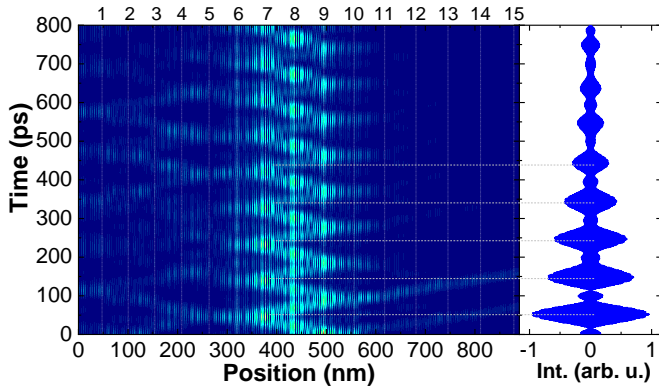


Figure 11: Left panel: simulated time evolution of the generated spectrum between 0.554 and 0.585 THz. The white vertical lines indicate the positions of the acoustic spacers. Right panel: experimental signal treated with a bandpass filter between 0.554 and 0.585 THz. Horizontal lines are a guide to the eye to relate the maxima in the detected signal with the localization of maxima of acoustic deformation in the structure. Adapted from Ref. 76.

To study the Bloch oscillations, we performed pump-probe coherent phonon generation experiments. We filter the measured time-trace to analyze an individual acoustic wave packet experiencing BOs, isolated from the ensemble of acoustic phonons oscillating within the whole structure (see Figure 11). We filtered the measured time trace using a bandpass filter between 554 and 585 GHz. This band comprises three peaks of the phononic WSL, which can be related to specific regions of the sample. Note that oscillations can be observed and have a very well-defined period of 95.3 ps, in agreement with the expected theoretical Bloch oscillations period τ of 92.7 ps. The left panel shows the simulated time evolution of the generated wavepacket.⁷⁶

3.3 Effective potentials for acoustic phonons

We have reported how a series of coupled cavities leads to the formation of minibands.⁵⁶ The miniband widths and the effective sound velocity in these structures can be engineered by the appropriate choice of the acoustic DBRs. Moreover, an effective phonon potential can be included in the structures by introducing a spatial variation of the cavity-mode energies.⁵⁶ The linear potential presented in the previous section is the simplest one.^{76,83}

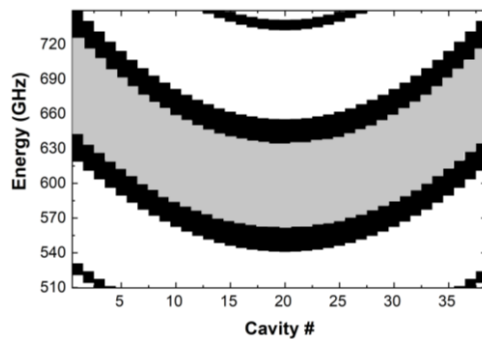


Figure 12: Allowed energy diagram of a parabolic acoustic phonon potential with building blocks consisting of GaAs spacers and 2.5 periods of GaAs/AlAs DBR. The cavity energies depend quadratically on cavity number with respect to the center of the structure, in such a way that the mode separation varies from $D = 0.24$ GHz at the bottom to $D = 8.87$ GHz at the edges of the structure. The gray region corresponds to the miniband originated in the coupling of cavity modes.

Parabolic potentials have been studied at length in electronics of quantum confined carriers and are usually associated with a spectrum of equidistant energy states. Figure 12 presents the allowed energy diagram of a parabolic acoustic-phonon potential.⁵⁶ The building blocks consist of GaAs spacers plus 2.5 periods of GaAs/AlAs DBR with stopband centered at the same energy of the cavity. The central cavity is tuned at 599.6 GHz, and the energy of the rest of the building blocks increases symmetrically to both sides with a parabolic dependence on cavity number. The mode separation varies from 0.24 GHz at the bottom to 8.87 GHz at the structure's edges. The introduced parabolic potential determines the structure's proper modes, as is clear from Figure 13, where both the acoustic reflectivity (right) and the phonon displacement distribution as a function of position and energy (left) are displayed.

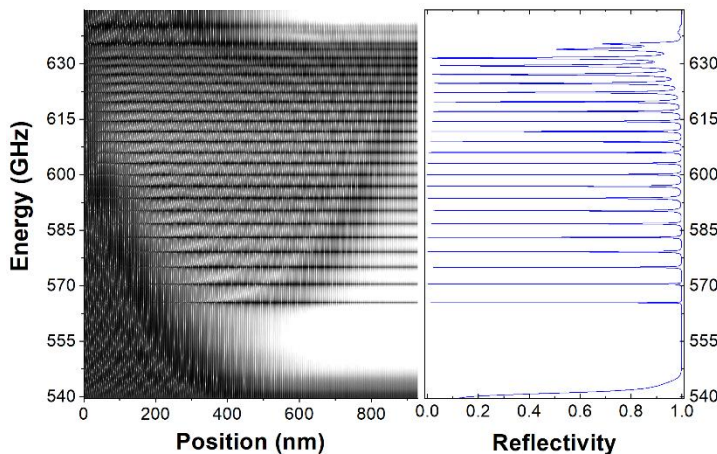


Figure 13: Acoustic reflectivity (right) and phonon displacement distribution as a function of position and energy (left) for the considered parabolic phonon potential. Darker regions indicate larger acoustic-phonon intensities. Adapted from Ref. 56.

For the left panel, the phonons have been calculated as incident from the left. Darker

regions indicate larger acoustic-phonon intensities. The acoustic energy can tunnel preferentially through the generated acoustic modes, leading to sharp dips in the acoustic reflectivity and the more intense phonon fields evidenced in the figure's left panel. Two critical aspects should be highlighted from this figure. First, the proper modes of the structure do not coincide with the energies of the cavities that make the device. The proper-mode energy separation does not grow linearly but, instead, decreases with increasing energy. Moreover, while the uncoupled cavity modes start at 599.6 GHz and grow up to 674.6 GHz, the proper modes cover a different energy range limited by 554.6 GHz and 644.6 GHz. As follows from Figure 12, this latter range corresponds to the portion of the allowed energy band limited from the bottom by the parabolic minigap region and from the top by the lower limit of the higher minigap branch. And secondly, in contrast to the case of electrons in a parabolic potential that displays an energy ladder that is linear with mode number N , i.e., the modes are equidistant, for acoustic phonons, this dependence goes as $N^{2/3}$. This behavior follows from the linear energy dispersion of acoustic phonons instead of quadratic with wave vector, as is the case of electrons.

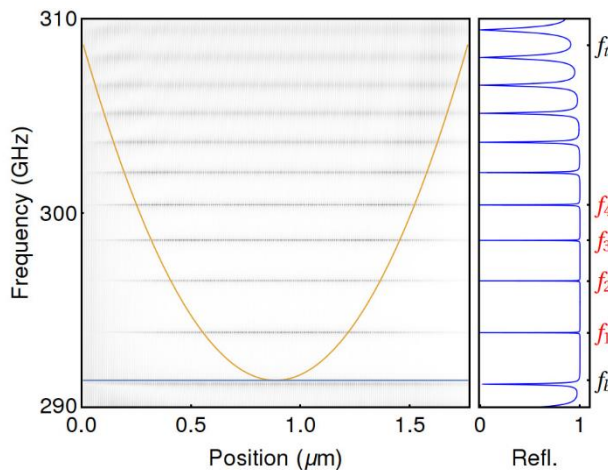


Figure 14: Allowed energy diagram of a parabolic acoustic phonon potential with building blocks consisting of GaAs spacers and 2.5 periods of GaAs/AlAs DBR. The cavity energies depend quadratically on the cavity number with respect to the center of the structure, in such a way that the mode separation varies from $D = 0.24$ GHz at the bottom to $D = 8.87$ GHz at the edges of the structure. The gray region corresponds to the miniband originated in the coupling of cavity modes. Adapted from Ref. 55.

The acoustic parabolic potential can also be implemented following the nearly free electron model approach.⁵⁵ In this case, we locally deform a SL to change the local band structure. To obtain a smooth, effective potential, we choose a structure composed of $N = 101$ cells and numerically define the structure parameters (period thickness and thickness ratio) to achieve the desired local band structure for each cell. In this case, the potential is defined by only the upper energy limit of the bandgap (orange line in Figure 14), as opposed to the case of the tight-binding approach where only the position of the effective bandgap (and not the width) is changed. It is also important to note that in the SL, the width of the bandgap imposes a limit on the bandwidth over which the potential is effective. By implementing potentials with a single superlattice, and due to the relatively overall thin structure, it is possible to experimentally realize complex potentials that are unrealistic with coupled nanocavities.

The effective potentials defined by design for the acoustic vibrations through the tuning of SLs or the energy of the cavity modes are entirely arbitrary. We reported linear and Morse potentials and single and double potential wells using the coupled-cavity and perturbed SLs approaches.^{55,56} The linear potential case gives rise to acoustic Bloch oscillations, briefly discussed in the previous section. The versatility of the multilayer-based nanoacoustic platform allows us to reproduce already known cases from other fields and explore new regimes and dynamics.

3.4 Band inversion and topological interface modes

Topological invariants have been widely used to describe the quantum Hall effect^{88–91}, electrically conducting polymers^{92,93}, and the conception of unidirectional optical waveguides^{94,95}. In periodic media, topological invariants allow for an efficient description of the information beyond the mere bandgap existence. For one-dimensional systems, the Zak phase⁹⁶, i.e., the one-dimensional Berry phase⁹⁷, is usually invoked as a topological number^{92,98–101}. For instance, the Zak phases corresponding to two concatenated

systems determine the existence of an interface mode confined between them. Such a mode is robust against perturbations in the systems that do not affect their Zak phases' values. First reports have recently merged these concepts from topology with acoustics in the kHz-MHz range^{98,102–106}. In this section, we introduce topological invariants to superlattice-based nanophononic systems.

One of the simplest realizations of the band inversion principle is depicted in Figure 15. We consider a GaAs/AIAs DBR with acoustic impedances $Z_{GaAs} = \rho_{GaAs}v_{GaAs}$ and $Z_{AlAs} = \rho_{AlAs}v_{AlAs}$. At a design frequency $f_0 = 175 \text{ GHz}$ the total acoustic path length of the unit cell is set to half a phonon wavelength $\lambda/2$, i.e. the thicknesses d of the two layers obey $\frac{d_{GaAs}}{v_{GaAs}} + \frac{d_{AlAs}}{v_{AlAs}} = \frac{1}{2f_0}$ and a phase of π is accumulated by a phonon at frequency f_0 traversing both layers of the cell.

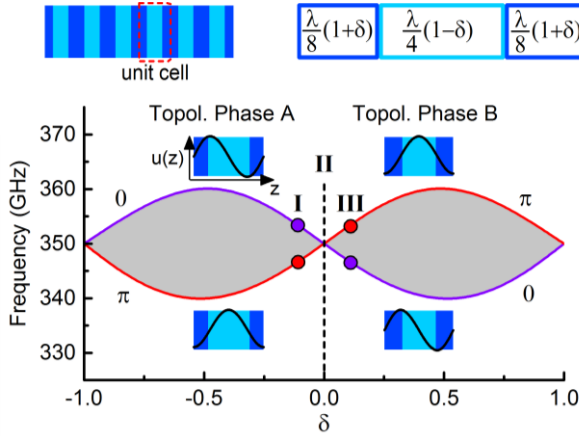


Figure 15: Band inversion and topological phases of a nanophononic DBR. (top) Schematic of a nanophononic DBR and its unit cell parametrized by δ which describes the relative thickness of the materials. Dark (light) shades correspond to GaAs (AIAs) layers. (bottom) Band inversion of the second acoustic minigap around 350 GHz. Shown are the frequencies of the band edges (violet and red) bounding the minigap (gray) as a function of the parameter δ . A sign change in δ marks the transition between the topological phases A and B of a DBR. While for $\delta < 0$ the Bloch mode at the lower (upper) band edge has a symmetric (antisymmetric) displacement pattern with respect to the centers of the material layers, these symmetries exchange for $\delta > 0$. The band edge modes are illustrated in the insets. Adapted from Ref. 58.

To describe how the overall acoustic path length is distributed between the two materials, we define a parameter $-1 < \delta < 1$ as sketched in Figure 15. Keeping f_0 constant, the thicknesses of the layers are $d_{GaAs} = \frac{v_{GaAs}}{4f_0}(1 + \delta)$ and $d_{AlAs} = \frac{v_{AlAs}}{4f_0}(1 - \delta)$. The particular case of a DBR made of $\lambda/4$ layers is therefore described by $\delta = 0$, which corresponds to a closed second minigap (see Figure 3).

We can follow the evolution of the width of the acoustic minigap when varying the value of δ continuously (shown in Figure 15). The violet and red lines indicate the frequencies of the two band edges enclosing the considered gap. In grey, the span of the minigap is indicated. Exactly at $\delta = 0$, the edge modes' symmetries undergo an inversion, marking a topological transition. A topological transition is usually characterized by topological invariants such as the Zak phase. The Zak phase of the acoustic bands can be computed by an integral across the Brillouin zone as follows⁹⁸:

$$\theta_{Zak}^n = \int_{-\pi/a}^{\pi/a} \left[i \int_{unit\ cell} \frac{1}{2\rho(z)v(z)^2} dz u_{n,k}^*(z) \partial_k u_{n,k}(z) \right] dk \quad (1)$$

Here, $u_{n,k}(z)$ is the mechanical displacement of the Bloch mode's cell-periodic part in the n -th band as a function of position z through the superlattice. As shown in Figure 15, the Zak phases corresponding to the phononic bands bounding the second minigap from the top and below appear inverted in energy when crossing the topological transition point at $\delta = 0$. It has been demonstrated that the Zak phases corresponding to the bands below a certain minigap are directly linked to the sign of reflection phase ϕ in that minigap.⁹⁹

For the second minigap (first minigap at the Brillouin zone center), the sign of the reflection phase is determined by the Zak phases of the zeroth and the first bands.⁹⁹

$$\text{sgn}[\phi] = \exp [i(\theta_{Zak}^0 + \theta_{Zak}^1)] \quad (2)$$

To establish the link between the band structure and the reflectivity properties of a DBR, we assume a semi-infinite DBR terminated at the center of a layer. Terminating the DBR at the center of a layer implies that the first unit cell is centrosymmetric, as sketched in Figure 15a. In this case, the connection between mode symmetries and reflection phases can be heuristically understood, since the anti-node (node) at the DBR surface results in a reflection phase ϕ evolving from 0 to π ($-\pi$ to 0) across the bandgap for $\delta < 0$ ($\delta > 0$). The sign of δ directly determines the sign of ϕ for frequencies inside the bandgap^{57,99}.

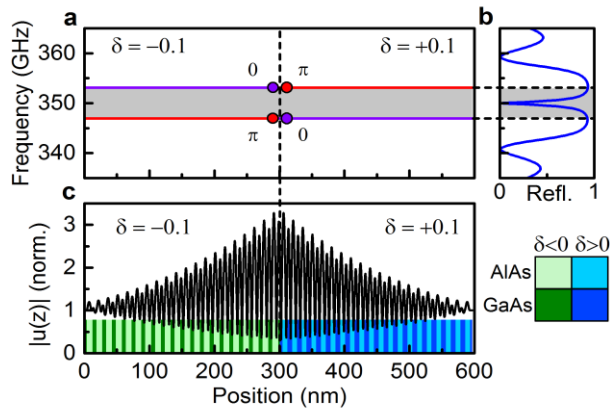


Figure 16: Topological interface state at 350 GHz. (a) Local phononic band diagram of two concatenated DBRs presenting inverted bands ($\delta = -0.1$ for the left DBR and $\delta = +0.1$ for the right DBR). Notice that the Zak phases and the mode symmetries are inverted at the interface. (b) Phonon reflectivity corresponding to the structure indicated in panel (a). Each DBR contains 20 centrosymmetric unit cells. The mode at 350 GHz corresponds to the topologically confined state, which appears at the center of the acoustic minigap. (c) Spatial displacement pattern $|u(z)|$ of the topological interface state at 350 GHz (black) together with the DBR structure. The mode envelope shows a maximum at the interface between the two DBRs and decays evanescently in both directions away from the interface. Green and blue color schemes denote spatial regions with different topological phases. Adapted from Ref. 58.

Consequently, by concatenating two DBRs with inverted bands as shown in Figure 16a, the first one with $\delta = -0.1$ and the second one with $\delta = +0.1$, the resonance condition –that is, the sum of the reflection phases equal to zero– is automatically fulfilled in the second minigap. Notice that the two DBRs present exchanged spatial mode symmetries at the band edges. Likewise, in the left DBR, the Zak phases of the bands bounding the second minigap are inverted with respect to the ones in the right DBR.

To prove the existence of topological states in real nanophononic systems, we performed all-optical Brillouin scattering measurements on a planar GaAs/AlAs sample with a layer structure as sketched in Figure 16 (c). The sample was grown by molecular beam epitaxy (MBE) on a (001) GaAs substrate and consisted of two parts: In the center, it contains two concatenated acoustic DBRs with 20 GaAs/AlAs bilayers each, designed for a frequency of $2f_0 = 354$ GHz and with inverted bands corresponding to the parameter choice $\delta = -0.1$ and $\delta = +0.1$ for the left and right DBR, respectively. This acoustic structure is enclosed by two GaAlAs-based optical DBRs designed for a wavelength of $\lambda_{opt} = 940$ nm such that the acoustic nanostructure serves as a $2\lambda_{opt}$ spacer of a resonant optical microcavity^{66,67,107}. A single Brillouin spectrum measured under double optical resonance condition (see Section 2.2.1 and references therein) is displayed in Figure 17 (top). Three clear peaks at 323 GHz (A), 360 GHz (B), and 397 GHz (C) can be observed. Peak B corresponds to the topological interface mode, while peaks A and C are phonons distributed along the DBRs generating Brillouin signals in a backscattering configuration. These peaks are

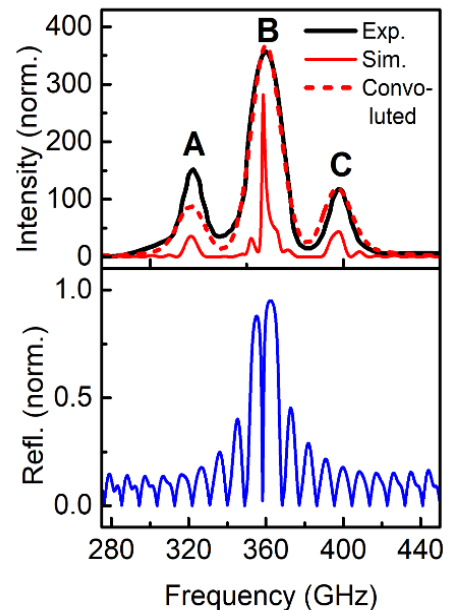


Figure 17: (top) Experimental Raman spectrum (solid black) together with photoelastic model calculation (solid red). The model calculation is convoluted with a Gaussian ($2\sigma = 13$ GHz) to account for the finite experimental resolution (dashed red). (bottom) Simulated acoustic reflectivity of the sample. The topological interface mode at 360 GHz corresponds to peak B in the Raman spectrum. Adapted from Ref. 58

a general feature of acoustic superlattices and samples formed by DBRs^{69,71,108,109}.

The simulated acoustic reflectivity of the studied sample is also shown in Figure 17 (bottom). The clear dip in the stopband around 360 GHz is generated by the topological interface mode between the two DBRs and can be assigned to the main peak (B) of the experimental spectrum. Notice that if the spatial mode symmetries of any of the two constituent DBRs are changed, this interface mode disappears, and the reflectivity would just show the stopband.⁵⁸ We also demonstrated the existence of these modes with higher resolution by performing asynchronous optical sampling pump-probe experiments.¹¹⁰

3.5 Discussion and conclusions

The low speed of sound and the long mean free path of acoustic phonons make the full phononic wave function information accessible to optical probes. With the availability of state-of-the-art nanofabrication technologies, engineered acoustic phonons constitute a versatile platform for investigating complex wave dynamics and localization.

In this chapter, we explored two strategies to simulate and implement potentials for acoustic phonons. The first one is based on the analogy of a confined mode in an acoustic cavity with the bounded state of a hydrogen atom. By concatenating multiple cavities, it is possible to simulate the effects of atomic chains, and in general, a tight-binding Hamiltonian. The second strategy consists of perturbing a periodic superlattice and changing the local band structure. By smoothly changing the thickness, structure, and composition of the unit cells in a periodic structure, it is possible to 'bend' the bands and simulate the effects of a potential for phonons.

Both strategies allow us to simulate the dynamics of acoustic phonons in a plethora of potentials. The implementation of the linear potential led to the experimental observation of Bloch oscillations for acoustic phonons.⁷⁶ A particular case at the edge of the tight-binding and the nearly free electron models appears when considering a coupled cavities system where the DBRs are just formed by just one layer of AIAs. In this case, the system can also be understood as a SL of unit cell $\lambda/5$ (AIAs) $4\lambda/5$ (GaAs). We treated this case of extremely thin DBRs using BTO/STO heterostructures forming a phononic molecule, and an array of coupled cavities displaying acoustic Bloch oscillations.⁸¹

The celebrated Su-Schrieffer-Heeger (SSH) model^{111,112} describes spin-polarized electrons on a one-dimensional lattice with staggered nearest-neighbor hopping in the tight-binding approximation, allowing the formation of topological solitons.^{113,114} The particular importance of the SSH model lies in its ability to provide a simple yet prototypical example of topological phase transitions in one dimension. By modulating the number of periods in the DBRs in a chain of concatenated acoustic nanocavities, it is possible to fully reproduce the physics of the SSH model in a nanoacoustic system, including the generation of edge states and monomer and trimer interface states.¹¹⁵

By applying the concept of band inversion to nanophononic periodic superlattices, we have successfully constructed and measured topological nanophononic interface states. We proposed a simple model to map the topological parameters to nanophononics. Contrary to a Fabry-Perot resonator, where two identical DBRs enclose a resonant spacer, the implemented resonator relies on two different DBRs without any spacer. This structure can also be associated with the SSH model.⁵⁸

The use of acoustic multilayers to study wave phenomena at the nanoscale can be further extended, considering novel materials in nanoacoustics and unexplored localization phenomena using acoustic phonons. Quasi-periodic systems have been investigated in photonics, where self-similar structures have demonstrated the possibility to engineer transport and localization properties. An example is a Fibonacci array that could be easily implemented for acoustic phonons with the advantage of exploring higher orders of the array. The Cantor sequence, another example of a self-similar structure, requires building structures

covering thicknesses of several orders of magnitude different. This can be implemented in nanoacoustic structures where it is possible to grow from sub-nm to several micrometer layers in the same structure. The almost linear dispersion of acoustics phonons allows straightforward modeling of the complex array structure dynamics.

Contributions related to this chapter

Theoretical prediction and experimental demonstration of Bloch oscillations of acoustic phonons in coupled cavity systems. Experimental demonstration of acoustic coupling effects in oxide heterostructures. Design and engineering principles for the conception of phononic potentials based on the tight-binding model (coupled cavities) and nearly-free electron models (bending of acoustic bands). Implementation of a variety of potentials, including parabolic, Morse, and linear potentials. Theoretical proposal for implementing topological modes in nanoacoustics and experimental demonstration of topological acoustic modes in the nanometer scale using two experimental techniques. Proposal of a simple and precise mapping of the SSH model into a nanoscopic acoustic system that allows unveiling the phonon dynamics of topologically confined modes and an experimental tool to characterize them.

- A. Phonon Bloch Oscillations in Acoustic-Cavity Structures
[N. D. Lanzillotti Kimura](#), A. Fainstein, and B. Jusserand
Phys. Rev. B **71**, 041305 (2005)
- B. Phonon Engineering with Acoustic Nanocavities: Theoretical Considerations on Phonon Molecules, Band Structures, and Acoustic Bloch Oscillations
[N. D. Lanzillotti-Kimura](#), A. Fainstein, C. A. Balseiro, and B. Jusserand
Phys. Rev. B **75**, 024301 (2007)
- C. Bloch Oscillations of THz Acoustic Phonons in Coupled Nanocavity Structures
[N. D. Lanzillotti-Kimura](#), A. Fainstein, B. Perrin, B. Jusserand, O. Mauguin, L. Largeau, and A. Lemaître
Phys. Rev. Lett. **104**, 197402 (2010)
- D. Nanomechanical Resonators Based on Adiabatic Periodicity-Breaking in a Superlattice
F. R. Lamberti, M. Esmann, A. Lemaître, C. Gomez Carbonell, O. Krebs, I. Favero, B. Jusserand, P. Senellart, L. Lanco, and [N. D. Lanzillotti-Kimura](#)
Appl. Phys. Lett. **111**, 173107 (2017)
- E. Acoustic Confinement Phenomena in Oxide Multifunctional Nanophononic Devices
A. E. Bruchhausen*, [N. D. Lanzillotti-Kimura*](#), B. Jusserand, A. Soukiasian, L. Xie, X. Q. Pan, T. Dekorsy, D. G. Schlom, and A. Fainstein
Phys. Rev. Mater. **2**, 106002 (2018)
- F. Topological Acoustics in Coupled Nanocavity Arrays
M. Esmann, F. R. Lamberti, A. Lemaître, and [N. D. Lanzillotti-Kimura](#)
Phys. Rev. B **98**, 161109 (2018)
- G. Coherent Generation and Detection of Acoustic Phonons in Topological Nanocavities
G. Arregui, O. Ortíz, M. Esmann, C. M. Sotomayor-Torres, C. Gomez-Carbonell, O. Mauguin, B. Perrin, A. Lemaître, P. D. García, and [N. D. Lanzillotti-Kimura](#)
APL Photonics **4**, 030805 (2019)
- H. Phonon Engineering with Superlattices: Generalized Nanomechanical Potentials
O. Ortíz, M. Esmann, and [N. D. Lanzillotti-Kimura](#)
Phys. Rev. B **100**, 085430 (2019)

Chapter 4

Opto-phononic co-localization in GaAs/AlAs multilayers

Fundamental observations in physics ranging from gravitational wave detection to laser cooling of a nanomechanical oscillator into its quantum ground state rely on the interaction between the optical and the mechanical degrees of freedom.^{8,10,116–123} A key parameter to engineer this interaction is the spatial overlap between the two fields, optimized in carefully designed resonators on a case-by-case basis.

In this chapter, we study optophononic structures based on GaAs/AlAs multilayers. Because of a remarkable coincidence in the physical parameters governing light and motion propagation in these two materials in one dimension, the equations for both longitudinal acoustic waves and normal-incidence light become practically equivalent for excitations of the same wavelength. This coincidence guarantees spatial overlap between the electromagnetic and displacement fields of specific photon-phonon energy pairs, leading to strong light-matter interactions and enabling nanoacoustics as a design knob in a plethora of optical and optoelectronic devices based on these materials.

4.1 GaAs/AlAs heterostructures as a platform for optophononics

Both optical and acoustic fields respond to similar wave equations in one dimension. In multilayered structures, the relevant design parameters are i) the speeds of light and sound that determine the photon and phonon wavelength, and ii) the contrast in the indices of refraction and acoustic impedances determining the reflection amplitudes and phases at each interface for light and sound, respectively.

GaAs and AlAs show a remarkable coincidence in nature that allows the conception and optimization of simultaneous optical and acoustic colocalized modes in one-dimensional multilayered structures. This coincidence consists of equal ratios for the speeds of sound v_i^{ac} and speeds of light v_i^{op} of the two materials^{124,125}, i.e.,

$$\frac{v_{GaAs}^{op}}{v_{AlAs}^{op}} \approx \frac{v_{GaAs}^{ac}}{v_{AlAs}^{ac}} = 0.84 \quad [1]$$

And at the same time, GaAs and AlAs present approximately equal ratios for the optical (n) and acoustic impedances (Z), i.e.,

$$\frac{n_{GaAs}}{n_{AlAs}} \approx \frac{Z_{GaAs}}{Z_{AlAs}} = 1.2 \quad [2]$$

In a given multilayered acoustic structure, for a given acoustic frequency f^{ac} , the thickness d_i of the layer i can be expressed as a function of the acoustic wavelength in the material i .

$$d_i = \alpha_i \lambda_i^{ac} = \alpha_i \frac{v_i^{ac}}{f^{ac}} \quad [3]$$

Equivalently, this thickness can be expressed in terms of optical wavelengths for a given optical frequency f^{op}

$$d_i = \beta_i \lambda_i^{op} = \beta_i \frac{v_i^{op}}{f^{op}} \quad [4]$$

For the particular optical frequency:

$$f^{op} = f^{ac} \frac{v_i^{op}}{v_i^{ac}} \quad [5]$$

The optical wavelength and the acoustic wavelength in the material i are equal:

$$\beta_i \lambda_i^{op} = \beta_i \frac{v_i^{op}}{f^{op}} = \beta_i \frac{v_i^{op} v_i^{ac}}{f^{ac} v_i^{op}} = \beta_i \lambda_i^{ac} \rightarrow \lambda_i^{op} = \lambda_i^{ac} \quad [6]$$

For the material j and the same frequencies f^{op} and f^{ac} , we observe that the optical and acoustic wavelengths are not the same:

$$\lambda_j^{ac} = \frac{v_j^{ac}}{f^{ac}} \quad [7]$$

$$\lambda_j^{op} = \frac{v_j^{op}}{f^{op}} = \frac{v_j^{op} v_i^{ac}}{f^{ac} v_i^{op}} = \lambda_i^{ac} \frac{v_j^{op}}{v_i^{op}} = \lambda_j^{ac} \frac{\lambda_i^{ac} v_j^{op}}{\lambda_j^{ac} v_i^{op}} \quad [8]$$

$$\lambda_j^{op} = \lambda_j^{ac} \left(\frac{v_i^{ac} v_j^{op}}{v_j^{ac} v_i^{op}} \right) \quad [9]$$

In general, choosing the optical and acoustic frequencies (f^{ac} and f^{op}) to match the optical and acoustic wavelengths in a given material implies that they do not match for any other material. For the specific case where:

$$\frac{v_i^{ac}}{v_j^{ac}} = \frac{v_i^{op}}{v_j^{op}} \quad [10]$$

then $\lambda_i^{op} = \lambda_i^{ac}$ and simultaneously $\lambda_j^{op} = \lambda_j^{ac}$. Comparing with Eqs. 1 and 10, we observe that this is precisely the case of GaAs/AlAs. In a multilayer, the contrast in the indices of refraction and the contrast of the acoustic impedances determine the reflection coefficients for light and sound, respectively. Looking at Eq. 2, the direct consequence is that for a GaAs/AlAs multilayer, the optical and acoustic reflectivities, and the modes' spatial profiles coincide.

As an illustration, let us consider the general case of an acoustic GaAs/AlAs multilayer

$$\alpha_1 \lambda_{GaAs}^{ac}; \alpha_2 \lambda_{AlAs}^{ac}; \alpha_3 \lambda_{GaAs}^{ac}; \dots; \alpha_{N1} \lambda_{GaAs}^{ac} \quad [11]$$

Due to the 'magic' coincidence in these materials, the same multilayer can be expressed as:

$$\alpha_1 \lambda_{GaAs}^{op}; \alpha_2 \lambda_{AlAs}^{op}; \alpha_3 \lambda_{GaAs}^{op}; \dots; \alpha_{N1} \lambda_{GaAs}^{op} \quad [12]$$

The situation would be radically different for another couple of materials:

$$\alpha_1 \lambda_X^{ac}; \alpha_2 \lambda_Y^{ac}; \alpha_3 \lambda_X^{ac}; \dots; \alpha_{N1} \lambda_X^{ac} \quad [13]$$

$$\alpha_1 \lambda_X^{op}; \alpha_2 \left(\frac{v_X^{op} v_Y^{ac}}{v_Y^{op} v_X^{ac}} \right) \lambda_Y^{op}; \alpha_3 \lambda_X^{op}; \dots; \alpha_{N1} \lambda_X^{op} \quad [14]$$

Where the number of acoustic and optical wavelengths in each layer is not the same. For instance, in the second layer, there are α_2 acoustic wavelengths, while $\alpha_2 \left(\frac{v_X^{op} v_Y^{ac}}{v_Y^{op} v_X^{ac}} \right)$ optical wavelengths. In the following section, we use GaAs/AlAs multilayers to study the simultaneous confinement of acoustic phonons and NIR photons in optimized Fabry-Perot resonators, topological interface resonators, and disordered superlattices.

4.2 Fabry-Perot resonators for light and sound

As a first example of how GaAs/AlAs can be used to colocalize light and sound, we analyze the case of a Fabry-Perot resonator based on two DBRs enclosing a spacer.

To demonstrate, experimentally and numerically, the simultaneous confinement of light and sound in an optimized resonator, we consider a $\lambda/2$ GaAs-spacer vertical microcavity enclosed by $(\text{Al}_{0.18}\text{Ga}_{0.82}\text{As}, \text{AlAs})$ ($\lambda/4, \lambda/4$) DBRs. We set 20 pairs on the bottom and 18 on top to partially compensate for the different reflectivities from the air and substrate sides.

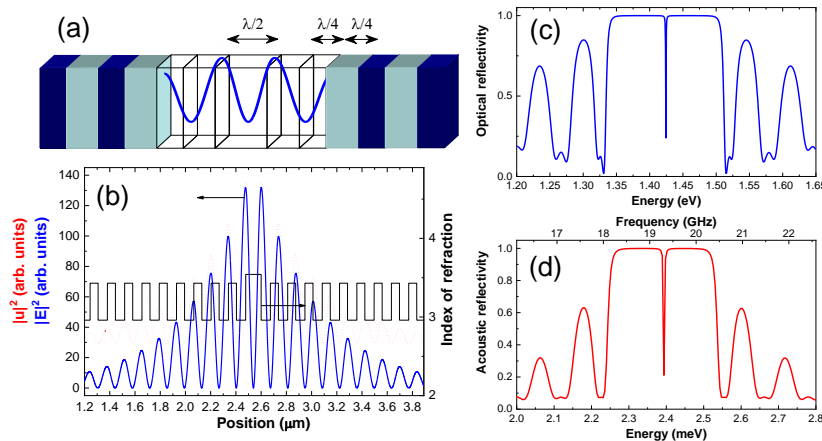


Figure 18: (a): Schematics of the GaAs photon-phonon microcavity. Dark regions represent AlGaAs, lighter ones AlAs. The number of layers does not correspond to the real structure. (b) Calculated photonic intensity (blue) and phononic displacement (red dotted curve, vertically shifted) distributions. The central five layers in panel (a) are transparent to display a detail of these curves. The thin lines in (b) represent the material refractive index. (c) and (d): Calculated optical and acoustic reflectivities, respectively. Adapted from Ref. 42.

The main consequence of the 'magic' opto-phononic coincidence of GaAs/AlAs is a simultaneous optimization of the light, and sound cavity modes are well centered within the corresponding reflectivity stopbands ($Q = 10^3$ for both light and sound), and both resonant optical intensity and square displacement are strongly amplified and precisely overlap at the cavity spacer.

Reflection-type pump-probe experiments⁵² were performed at room temperature with laser wavelength $\lambda=870$ nm in resonance with the absorption edge of the GaAs spacer. The optomechanical cavity thus involves electronic resonances in the light-matter processes, in addition to the optical and acoustic resonances. Picosecond pulses (~ 1 ps, 870 nm) from a mode-locked Ti:sapphire laser were split into the pump (1–300 mW) and probe (typically 1 mW) pulses. Photon pulses of 1 ps are chosen so that their spectral width matches the finesse of the optical cavity ~ 0.8 nm). The laser was tuned in resonance with the optical cavity mode to enhance the impulsive generation of phonons. The probe laser angle is set so that its energy is tuned to the flank of the optical cavity mode to maximize the detection sensitivity.⁷¹ Note that the laser energy is well within the transparency region of the materials forming the DBRs (gap AlAs ~ 415 nm and gap $\text{Al}_{0.18}\text{Ga}_{0.82}\text{As}\sim 780$ nm). Consequently, the impulsive phonon generation occurs mainly at the GaAs cavity spacer. The photoelastic component of the detection is strongly enhanced at resonance selectively at the GaAs spacer.^{69,125–127}

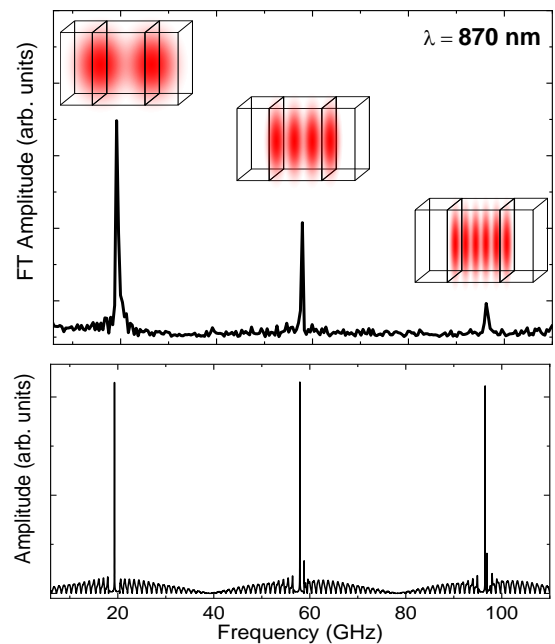


Figure 19: Top: Amplitude of the Fourier transform for the full 0–3000-ps experimental timewindow). The spatial displacements associated with these modes are depicted in the shown insets. Bottom: Calculated generated spectrum. Adapted from Ref. 42.

To identify these modes, Figure 19(top) displays the Fourier transform amplitude of the measured time trace (integrated for all measured times). Three spectrally narrow peaks are observed at around 20 GHz, 60 GHz, and 100 GHz. The width of the modes is determined by the experimental time window (0- 3 ns), and it is not reflecting the mode lifetime. Figure 19 (bottom) presents the calculated generated spectral amplitude, considering an impulsive (instantaneous) strain localized at the cavity layer.⁷¹ No fitting parameters are used; only nominal thicknesses and published material properties. Three main ultranarrow peaks appear at the same frequencies as the experiment, corresponding to the first three (odd order) acoustic modes confined in the microcavity. The even-order phonon cavity modes have an odd (with respect to the center) strain distribution at the cavity spacer and are thus forbidden by parity (the photon field intensity is even).

These enhanced interactions enable the study of other interesting phenomena in the co-localization regime, for example, slow-light and slow-phonons,¹²⁸ the optical cavity dynamics after an ultrafast excitation,^{129,130} or even the study of tripartite systems combining NIR photons, acoustic phonons, and excitonic/polaritonic systems.¹³¹

4.3 Optophononic topological modes

We generate an interface mode inside a bandgap by concatenating two periodic lattices with inverted bands. The existence of this interface state is protected against any perturbation that does not change the underlying topological invariants of the structures. The robustness of these topologically induced interface modes has been exploited in a wide range of physical systems^{58,110,132–134} for a single type of excitations (e.g., photons^{134–138}, plasmons¹³², phonons^{58,110,115}, vibrations^{133,139}, polaritons^{140,141}, classical acoustics^{133,142–147}). In this section, we introduce the concept of two perfectly colocalized fields -optical and acoustic- presenting a topologically confined mode on the same physical platform.

To generate an interface mode through band inversion, we concatenate two DBRs with the following conditions: 1. They share a common bandgap (same central frequency, same bandwidth) 2. The order of Bloch mode symmetries at the band edges enclosing this bandgap is inverted. Under these conditions, the reflection phases of the two DBRs present opposite signs. This effect is directly rooted in the opposite topological properties of the individual bands and can be expressed in terms of the Zak phase^{58,133,146}. At the bandgap center, the phases are equal in magnitude, resulting in a zero roundtrip phase, thus giving rise to a resonance.

In a superlattice, the parameter δ , determining the topological phase (See Chapter 3) is equally describing the optical and the acoustic DBR. As such, a band inversion characterized by a sign change of δ happens simultaneously in the optical and acoustic domains (see Figure 20). Concatenating two superlattices (DBR)

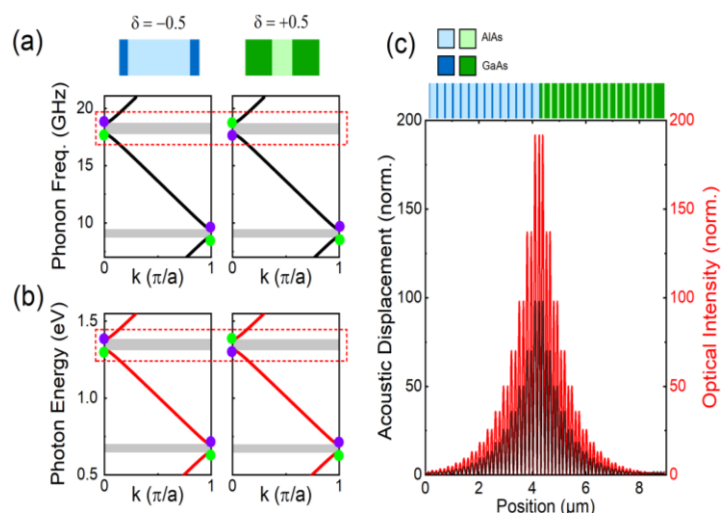


Figure 20: Construction principle of an interface state in a photonic-phononic nanocavity by band inversion. (a) Schematic of the unit cells of each DBR parametrized by δ , which describes the relative thickness of the materials. Dark (light) colors represent GaAs (AlAs), blue and green are used to distinguish between left and right superlattices, respectively. The dispersion relations of acoustic phonons (a) and photons (b) present inverted Bloch mode symmetries around the first band gap at the Brillouin zone center. The dashed red box indicates the bandgap over which the band inversion takes place, mode symmetries are indicated with violet (antisymmetric) and green (symmetric) dots. (c) The spatial displacement pattern $|u(z)|^2$ (black) and the optical profile $|E(z)|^2$ (red) of the topological interface state at 18.12 GHz/1.34eV are colocalized and present a maximum at the interface between the two DBRs. Both fields decay evanescently away from the interface. The complete heterostructure is represented on top of panel (c). Adapted from Ref. 148.

presenting opposite signs of δ will thus result in an interface optophononic mode. As in the case of the Fabry-Perot resonator, we observe a clear spatial overlap between the phononic and the optical modes.

To evidence the optical interface mode, we performed optical reflectivity measurements. Figure 21 shows the reflectivity of the structure measured by FTIR spectrometry. The two measured stop bands around 0.71 eV and 1.34 eV correspond to the first and second bandgap illustrated in Figure 20. The dip in the middle of the second bandgap is associated with an optical cavity mode. The simulated optical reflectivity (grey lines) using a transfer matrix formalism agrees with the experimental observations. The difference in the linewidth observed between experiments and theory is mainly due to the gradient present in the sample to allow a position-dependent resonance.

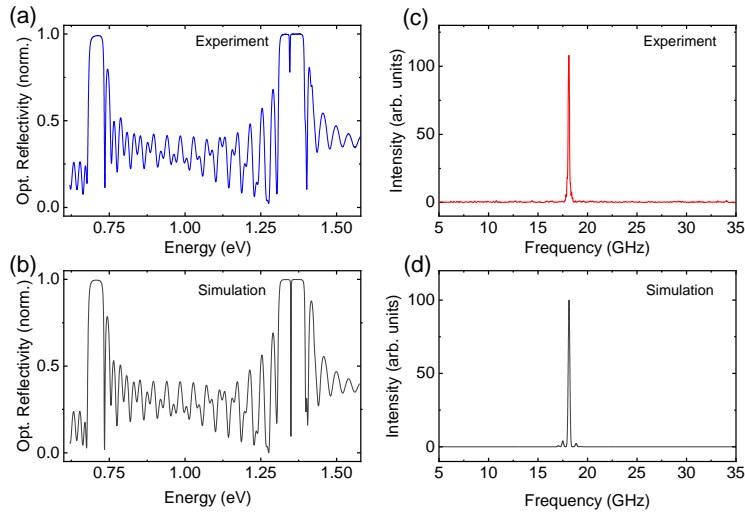


Figure 21: Optophononic topological mode. (a) Continuous wave optical characterization of the topological interface modes. The measured optical reflectivity reveals an interface state in the middle of the first optical stopband at the Brillouin zone center. (b) Transfer matrix calculation of the optical reflectivity (c) Fast Fourier transform (FFT) of the experimental time trace featuring the topological resonator mode at 18.12 GHz. (d) Photoelastic model calculation of the pump-probe spectrum considering a resolution of 90MHz. Adapted from Ref. 148.

linewidth of 90 MHz), the interference between phonons generated by two consecutive pump pulses, and lower signal detection efficiency for long delays.¹⁴⁸

By following the same design principle, we can define a full class of resonators, consisting of two DBRs presenting inverted bands and centrosymmetric unit cells. By comparing different combinations of concatenated superlattices, it can be demonstrated that despite similar Q-factors, the Brillouin cross-section varies over a broad range of values but never matches the performance of the Fabry-Perot resonators.¹⁴⁸

4.4 Anderson localization in perturbed superlattices

Examples of scattering in the presence of disorder appear in several physics fields, ranging from the diffusion of light passing through the dust to the dynamics of acoustic waves in the presence of obstacles. Diffusion halts when the scale of coherent multiple scattering is reduced to the wavelength itself, this being ascribed to the (Anderson) localization of the eigenmodes' wave functions. The transition to the Anderson localization regime is inherent to any system described by a wave equation in a disordered medium.^{149–154}

Using disorder is thus an alternative strategy to confine light and sound at the nanoscale. Moreover, the co-localization warranted by the GaAs/AlAs could be the base of an efficient probe to test the Anderson localization of acoustic phonons at the nanoscale.

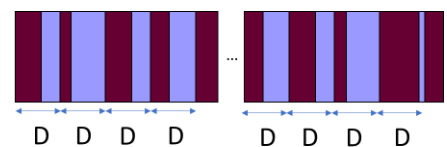


Figure 22: Schematics of the considered multilayered structure to observe the colocalization of light and sound in disordered systems.

To theoretically test the co-localization concept in disordered systems, we use a DBR with a unit cell formed by a (GaAs/AlAs) of a thickness (61.88 nm/73.48 nm) forming a ($\lambda/4, \lambda/4$) SL. This structure simultaneously opens a maximum-width first order bandgap with a center frequency of 344.6 THz ($\lambda = 870$ nm) for near-infrared photons and 19 GHz for acoustic phonons. We introduce geometrical disorder in the position of the interface between the two materials with a Gaussian distribution. The standard deviation σ determines the level of disorder, while the period D remains constant.

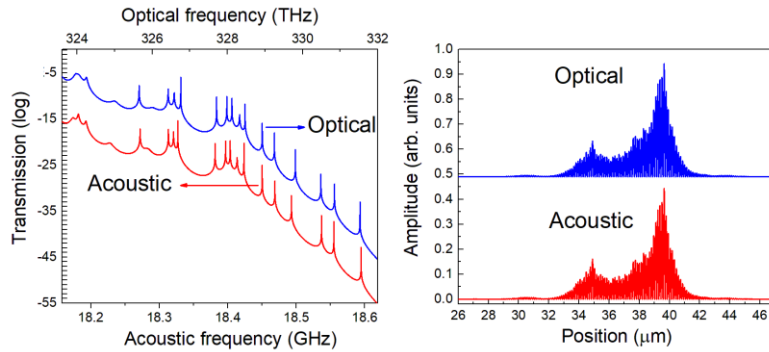


Figure 23: Optical and acoustic transmission spectra of a disordered GaAs=AlAs superlattice with $d_1=61.88$ nm, $d_2=73.48$ nm, $N=600$, and $\sigma=0.15D$ at the low-frequency optical and mechanical band-gap edges. The energy density of the displacement and the electric fields of the highlighted pair in left panel are plotted in the right panel, showing perfect spatial colocalization. Adapted from Ref. 155.

Figure 23 shows the acoustic and optical transmission spectra around the first-order odd bandgap of a disordered superlattice formed by 600 periods for a value $\sigma=0.15D$. There is a remarkable correspondence between both spectra, where a factor of ~ 17800 (the ratio between the speeds of light and sound in GaAs) has rescaled the energy axes.

We show the mechanical displacement profile and the electrical field distribution of an arbitrary opto-phononic mode in the right panel.

Remarkably, there is a perfect spatial co-localization. As in the Fabry-Perot resonator and the topological interface modes, this co-localization enhances the Brillouin interactions and the coherent phonon generation and detection processes.¹⁵⁵

4.5 Discussion and conclusions

In this chapter, we showed how a unique characteristic of the GaAs/AlAs couple of materials results in the co-localization of light and sound in multilayered nanostructures. This co-localization takes place also when using alloys of these two materials. Whenever a microcavity is optimized to confine light in the NIR, the same structure behaves as an optimized acoustic cavity for ~ 18 GHz. Since GaAs and AlAs heterostructures are widely used in optoelectronics and photonics, the engineering of acoustic phonons becomes directly accessible in existing structures. The co-localization of the two fields results in enhancement factors of $\sim 10^6$ in the pump-probe signals.

The coincidence between the electric field and the acoustic displacement implies that the electric field is dephased from the strain field. As a consequence, every system that optimizes a coupling with the maximum of the electrical field would present no interaction with the strain. A clear example of this situation is the exciton-polariton systems, where a quantum well is localized at the maximum of the electrical field in an optical cavity. In this case, the quantum well usually matches the position of a node of the strain. Thus, the strain does not affect the physics of the polaritonic system. However, placing the quantum well in a different position where both electric and strain fields are non-zero would enable the engineering of the phonon-polariton interaction. The same principle would be valid for a quantum emitter interacting with both the electrical and strain fields.¹³¹

In the conception of simultaneous optical-acoustic topological interface states, the local density of states of two excitations can be engineered and controlled simultaneously. As such, topological engineering can be performed not only on the individual excitations but also on their interactions, taking advantage of different robustness characteristics.¹⁴⁸

In the last section of this chapter, we showed that the co-localization is present even in disordered superlattices and does not require any kind of periodicity in the system. The possibility of engineering opto-

phononic systems is at the base of a new generation of modulated light sources, state-of-the-art optomechanical resonators, and structures where light-matter interactions can be manipulated.

Contributions related to this chapter

Theoretical proposal and experimentally demonstration that GaAs/AlAs microcavities designed to confine photons are automatically optimized to confine acoustic phonons of the same wavelength, strongly enhancing their interaction. Observation of optomechanical coupling at sub-THz acoustic frequencies in these monolithic devices bridging the gap between optomechanics and optoelectronics. Observation of slow acoustic and optical modes and dynamics of the interaction between confined colocalized fields. Extension of the concept of light-sound co-localization in GaAs/AlAs to more general structures such as topological interface modes based on the same design principle. Numerical demonstration of the co-localization of light and phonons in disordered superlattices in the Anderson regime.

- A. Strong Optical-Mechanical Coupling in a Vertical GaAs/AlAs Microcavity for Subterahertz Phonons and Near-Infrared Light
A. Fainstein, [N. D. Lanzillotti-Kimura](#), B. Jusserand, and B. Perrin
Phys. Rev. Lett. **110**, 037403 (2013)
- B. Towards GHz–THz Cavity Optomechanics in DBR-Based Semiconductor Resonators
[N. D. Lanzillotti-Kimura](#), A. Fainstein, and B. Jusserand
Ultrasonics **56**, 80 (2015)
- C. Dynamical Optical Tuning of the Coherent Phonon Detection Sensitivity in DBR-Based GaAs Optomechanical Resonators
P. Sesin, P. Soubelet, V. Villafañe, A. E. Bruchhausen, B. Jusserand, A. Lemaître, [N. D. Lanzillotti-Kimura](#), and A. Fainstein
Phys. Rev. B **92**, 075307 (2015)
- D. Slow Light and Slow Acoustic Phonons in Optophononic Resonators
V. Villafañe, P. Soubelet, A. E. Bruchhausen, [N. D. Lanzillotti-Kimura](#), B. Jusserand, A. Lemaître, and A. Fainstein
Phys. Rev. B **94**, 205308 (2016)
- E. A Topological View on Optical and Phononic Fabry–Perot Microcavities through the Su–Schrieffer–Heeger Model
M. Esmann and [N. D. Lanzillotti-Kimura](#)
Appl. Sci. **8**, 527 (2018)
- F. Anderson Photon-Phonon Colocalization in Certain Random Superlattices
G. Arregui, [N. D. Lanzillotti-Kimura](#), C. M. Sotomayor-Torres, and P. D. García
Phys. Rev. Lett. **122**, 043903 (2019)
- G. Topological Optical and Phononic Interface Mode by Simultaneous Band Inversion
O. Ortiz, P. Priya, A. Rodriguez, A. Lemaitre, M. Esmann, and [N. D. Lanzillotti-Kimura](#)
Optica **8**, 598 (2021)

Chapter 5

Optophononic micropillars and acousto-plasmonic metasurfaces

In the previous chapters, we showed how the confinement and propagation properties of acoustic phonons could be tailored in one dimension using nanometric multilayered structures. In this chapter, we address the three-dimensional confinement properties in nanostructures. First, we describe semiconductor optophononic micropillars based on GaAs/AlAs multilayers and how they can be measured and integrated with other optical systems. Then, we introduce plasmonic antennas forming metasurfaces as versatile and efficient coherent-phonon generators and detectors.

Micropillar cavities confine light in the three directions of space, and they are widely used in non-linear optics taking advantage of the strong optical non-linearities in GaAs/AlAs semiconductors,^{156–158} in optical simulations based on exciton-polaritons,^{61,159–161} and in solid-state quantum optics where single quantum dots constitute highly coherent artificial atoms.^{60,162} As we noted in Chapter 4, GaAs/AlAs devices form an attractive platform for optomechanical applications due to the simultaneous confinement of light and phonons in the same structure. In the first part of this chapter, we introduce the main ideas and results related to micropillar cavities working as optophononic resonators confining both optical and mechanical fields.

One of the critical challenges in nanoacoustics is counting with transducers able to generate phonons with different frequencies on demand. Standard metallic thin-film transducers have associated a fixed spectrum, limiting the range of applications.^{2,52,53} Even more complex devices like multilayers, optical microcavities, metallic nanoparticles, and semiconductor quantum dots fall into this category of a single-fixed generation spectrum.^{17,37,124,127} Plasmonics¹⁶³ brings an interesting new approach to this nanophononics challenge by introducing the polarization degree of freedom.

Plasmonics revolutionized the fields of optics during the last 20 years. The possibility of confining and controlling optical fields in the subwavelength regime^{164–166} opens a myriad of applications.^{163,167–170} There is, however, one usual main drawback in plasmonics. The resonances are intimately related to high absorption cross-sections, severing the number of applications. The coherent phonon transduction requires localized optical fields in small volumes, and strong absorption is highly desirable. Nanoantennas^{171–173} present strong resonances that are extremely sensitive to polarization and well-defined acoustic modes. The use of plasmonic structures as transducers to generate acoustic phonons or the use of acoustic phonons to study plasmonic nanostructures is relatively new, and only a few works have explored these possibilities.^{4,17,174–177} In the second part of this chapter, we introduce the engineering of acousto-plasmonic metasurfaces.

5.1 Semiconductor micropillars as optophononic resonators

A standard optical micropillar cavity is formed by two DBRs enclosing a spacer in the vertical direction, with the shape of a cylinder.^{62,178} The optical field is confined in the vertical direction due to the DBRs, while in the lateral direction is confined by the contrast between the indices of refraction of the semiconductors and the air, similar to the confinement observed in an optical fiber.

The acoustic behavior of micropillars has been less investigated. While the mechanism governing the acoustic confinement along the pillar axis is very similar to the optical confinement, the Poisson's ratio (i.e., the signed ratio of transverse elastic strain to axial elastic strain) and a different set of boundary conditions (free surfaces) lead to very different acoustic/optical confinement in the transverse direction (see Figure 24). Despite the additional radial modulation of the field, the overlap between the optical and mechanical modes is still remarkable.¹⁷⁹

The optomechanical coupling factors reach values of approximately 10^6 rad/s, the mechanical quality factors (Q) exceed 10^3 , and the maximal products of Q times frequency are in the order of 10^{14} Hz, revealing the potential of micropillars as ideal optomechanical resonators. In addition, it is possible to optimize the coupling of quantum emitters to this optomechanical platform.^{179,180}

Finally, a full understanding of the three-dimensional confinement of acoustic phonons in micropillars opens the possibility of actually engineering the phononic landscape of nanostructures where quantum emitters such as InGaAs quantum dots and quantum wells can be integrated. This enables an entirely novel feature to the quantum information toolbox: the control of the interactions in a tripartite system constituted by a confined optical field, a confined mechanical mode, and an electronic excitation.^{131,181}

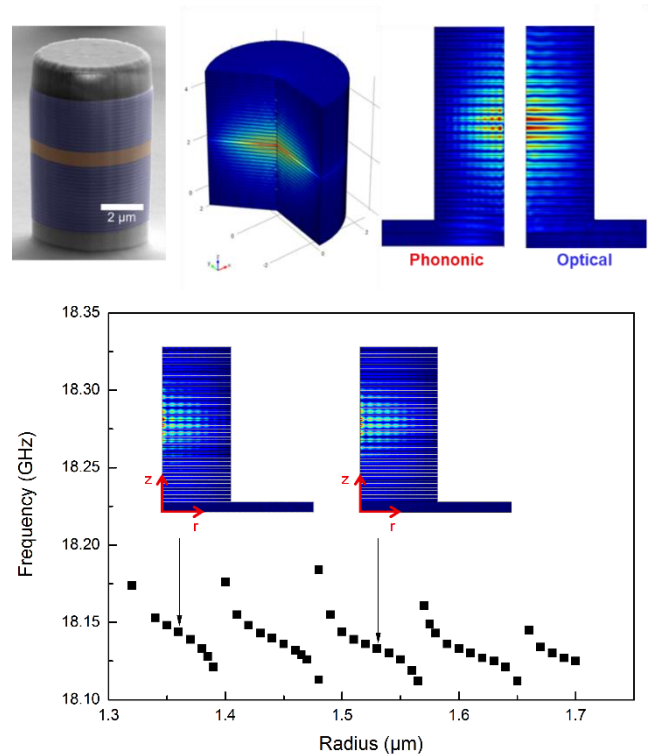


Figure 24: Optomechanical pillar microcavity. Top: (a) SEM micrograph of a micropillar structure, formed by two distributed Bragg reflectors embedding a spacer. (b) Finite elements simulation of the electromagnetic fundamental mode in a micropillar. (c) Modulus square of the electric field distribution in a 10 periods/DBR resonator of $1.5 \mu\text{m}$ radius with a $\lambda/2$ cavity, for a mode of 921 nm of optical wavelength. Modulus square of the mechanical displacement distribution corresponding to the confined acoustic mode at a resonance frequency of 18.2 GHz . Note the vertical modulation matching the one shown in (b), in addition to the radial modulation due to the free surface boundary condition. Bottom: Dependence of the fundamental confined acoustic mode frequencies on the radius of the micropillar. The multiple anticrossings in the mechanical dependence originate from the coupling of vertical and radial modes due to the Poisson's ratio.

5.2 Brillouin scattering in nested micropillar resonators

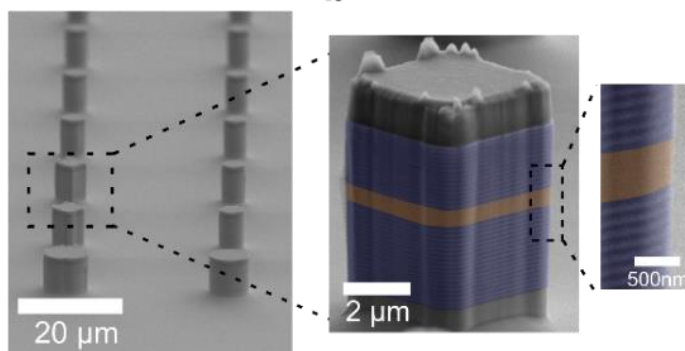


Figure 25: SEM images of (left) an array of circular and square micropillar resonators, and (right) a single square micropillar with a lateral extent of $4.5 \mu\text{m}$. The top layer is SiN deposited as part of dry etching. The inset shows a detail of the DBR and spacer layers in false colors.

fabricated by optical lithography and inductively coupled plasma etching. We show scanning electron microscope (SEM) images of an array of micropillar resonators and a zoomed-in view of a single square

In this section, we study a monolithic semiconductor device for the versatile generation of tailored ultrahigh-frequency Brillouin signals. The device is based on an optical semiconductor micropillar cavity embedding an ultrahigh-frequency nanoacoustic resonator. This nested three-dimensional architecture allows an independent design of its optical and acoustic properties.¹⁸²

From the planar optophononic cavities, $30 \mu\text{m}$ pitched arrays of square and circular micropillars with various lateral sizes are

micropillar with a lateral extent of $4.5\ \mu\text{m}$ in Figure 25, respectively. In the particular case of Figure 25 (right), an acoustic resonator (yellow) with a confined mode at 300 GHz is nested in the optical cavity.

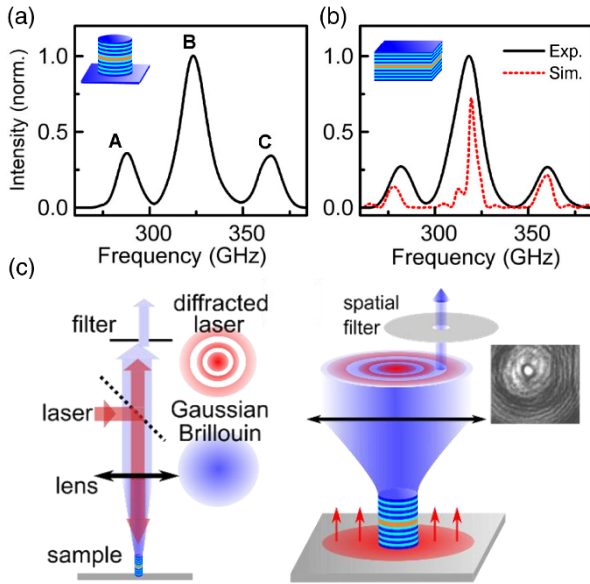


Figure 26: Anti-Stokes Brillouin spectrum measured on the studied micropillar resonator. The spectrum exhibits three pronounced peaks (A–C). (b) Brillouin spectrum measured on a planar resonator with an identical vertical structure (solid black curve). A photoelastic model calculation (dashed red curve) well accounts for the three-peaked structure of the spectrum. (c) Setup in reflection geometry: the reflected optical signal comprises a pronounced pattern of diffracted laser light (red) and the Brillouin beam (blue) with a Gaussian spatial pattern dictated by the optical micropillar modes. A spatial filter optimizes the relative collection ratio of the Brillouin signal. The inset shows the corresponding experimental diffraction pattern.

around 280, 320, and 360 GHz, labeled A, B, and C, respectively. Peak B corresponds to the confined mode in the acoustic resonator, while peaks A and C are peaks associated with the DBRs usually measured under backscattering geometry. Figure 26(b) shows the spectrum measured on a planar structure showing similar features.

Using this measuring scheme, we have demonstrated¹⁸² that one can exploit the heating effects induced by the excitation laser to lock the optical cavity mode at a given spectral position for a given power. This effect is particularly evident in the case of micropillars due to the limited heat release capacity towards the substrate. We used this effect to optimize the Brillouin scattering signal by initially detuning the excitation laser from the unperturbed cavity mode.¹⁸²

5.3 Coherent phonon generation in optophononic micropillars

To study the phonon dynamics in micropillars, we implemented a time-resolved differential optical reflectivity (pump-probe) measurement^{52,53} with micrometer lateral spatial resolution. The resolution is $\sim 5\ \mu\text{m}$, implying that we address single pillars in the experiments. A 4-picosecond optical pump pulse generates coherent mechanical vibrations. The changes induced in the shape and the indices of refraction of the micropillar are then probed by measuring the optical reflectivity of a delayed second pulse. By changing the delay between the pump and probe pulses, we reconstruct the time evolution of the optical reflectivity modulated by the mechanical vibrations, as shown in Figure 27.

The studied pillars are designed to operate at $\sim 18\ \text{GHz}$ mechanical frequency and $900\ \text{nm}$ for the optical mode, close to the GaAs energy gap at room temperature to enhance the optomechanical response.^{12,125}

Confined acoustic modes are observed at ~ 18 and ~ 55 GHz with room temperature mechanical quality factors in the 200 to 1600 range.

Figure 27 presents a typical signal measured on a 5 μm pillar. The left panel displays the as-measured differential reflectivity as a function of the delay t between the pump and probe pulses. This signal is dominated by the electronic contribution at a short delay and by the mechanical one at long time delays. The spectrum obtained from the Fourier transform between 0 and 10 ns is shown in the right panel.

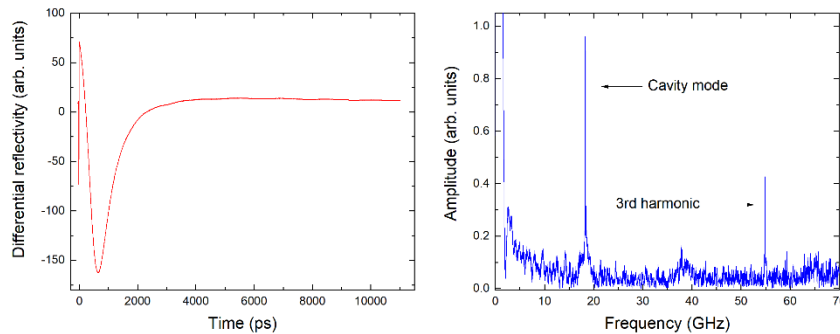


Figure 27: (left) Differential reflectivity time trace of the micropillar resonator. (right) Fast Fourier transform (FFT) of the experimental time traces featuring the acoustic resonances at 18.3, 54.9 GHz, with a FWHM of 84 and 90 MHz, respectively.

Two mechanical resonances are observed at 18.3 and 54.9 GHz. Because the pump-induced perturbation is concentrated in the GaAs-spacer layer, the generated localized strain mainly corresponds to vibrations vertically confined in the cavity. The observed resonances correspond to the fundamental mode and the third overtone. The absence of even order gaps for $\lambda/4$, $\lambda/4$

mirrors prevents the existence of even order acoustic modes confined in the vertical direction, similar to what happens in planar structures (see Chapter 4).

Using micropillars, we can study confinement effects and phonon dynamics,¹²⁹ and the optical tuning based on thermal and electronic recombination effects¹³⁰, and demonstrate record high values of the Qxf indicator, a figure of merit that allows evaluating the maximum number of quantum operations that can be achieved. The reached values of $\sim 10^{14}$ at room temperature is a breakthrough in the field.¹²⁹

5.4 Towards fiber-integrated nanophononics

Coherent phonon generation experiments rely on the optical mode matching between the incident pump and probe laser fields and the optical modes of the structure under study. The efficient generation of coherent acoustic phonons relies on an efficient coupling of the pump field into the system, while the sensitive detection of phonons requires an efficient coupling of the probe to the optical mode undergoing a phonon-induced modulation. The main practical challenges for the actual implementation of this technique are, therefore: 1) stability, 2) reproducibility, and 3) high power densities limiting the range of compatible samples¹⁸³.

To address these issues, we integrate single-mode optical fibers with optophononic micropillars cavities. The mode-overlap of the fiber to the microresonators achieved during the gluing is permanent and stable, eliminating the need for focalization optics and any further beam realignment, providing the means to perform reproducible plug-and-play experiments.

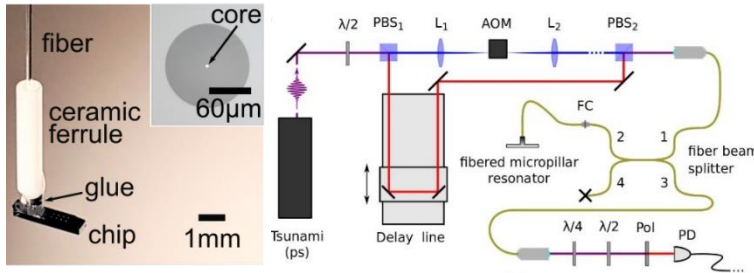


Figure 28: (left) Final device with one individual micropillar on the chip coupled to the single mode fiber. A ceramic ferrule provides additional mechanical stability. Inset: microscope image of fiber core and cladding. (right) Schematic of the pump-probe setup used to characterize the optophononic response of fiber-coupled microcavities. We replaced the standard focalization optics by a fibered system. PBS, L, AOM, FC, Pol and PD stand for polarizing beam splitter, lens, acousto-optic modulator, fiber coupler, linear polarizer and photodetector, respectively.

28(left) presents a picture of a finished device. A ceramic ferrule (white tube) provides additional mechanical stability.

Our measurement setup for the integrated samples is based on a fiber beam splitter (see schematics in Figure 28-right). The fiber-coupled microresonators confine ~ 20 GHz phonons and NIR photons. Figure 29 shows the differential time-resolved reflectivity (top) and the Fast Fourier Transform of the signal (bottom) measured on a fibered micropillar. The spectrum shows clear peaks at 18.3, 54.9, 91.5, and 128 GHz, corresponding to the fundamental mode and 3rd, 5th, and 7th harmonics of the resonator. In these picosecond ultrasonic pump-probe experiments, we measured acoustic phonon signals at remarkably small excitation powers of $1\mu\text{W}$, with signals that remain stable for longer than 48 hours.

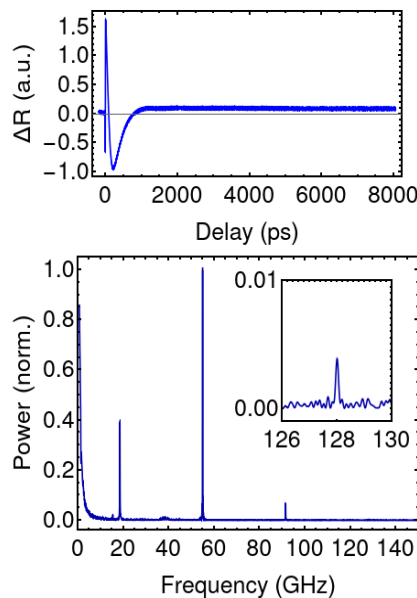


Figure 29: (top) Differential reflectivity time trace of the micropillar resonator. (bottom) Fast Fourier transform (FFT) of the experimental time traces featuring the acoustic resonances at 18.3, 54.9, 91.5 and 128 GHz. The inset shows a zoom around the seventh harmonic

5.5 Polarization-controlled acousto-plasmonic metasurfaces

Metasurfaces can control electromagnetic wavefronts and enhance light-matter interactions.¹⁷⁰ Therefore, they enable the control of the interaction between the light and phonons in the nanostructures. In this section, we show how an optimized plasmonic metasurface can be used as a light-phonon transducer with characteristic phonon frequencies selected by the laser polarization. The samples studied in this section are metasurfaces formed by periodic arrays of metallic-bar resonators. The plasmonic resonators are the

fundamental building blocks of the metasurface and determine both the optical and acoustic resonances. We fabricated the samples by standard e-beam lithography, metal evaporation, and lift-off techniques.

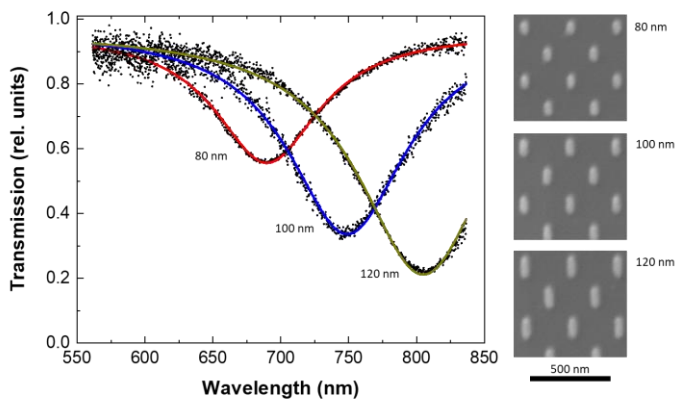


Figure 30: (left) Measured optical transmission of the three control metasurfaces. The transmission for the vertical polarization is plotted in red, blue and green for the 80 nm, 100 nm, 120 nm bars. (right) Scanning electron microographies of the metasurfaces.

metasurface is transparent. This fact has a crucial consequence for the pump-probe experiments.

To explain how the polarization can be linked to a selective phonon generation, we fabricated three control samples, each one consisting of an array of parallel nanoantennas (see Figure 30).

The antenna lengths determine the optical resonances with a strong polarization dependence. When an incident laser has a parallel polarization to the main axis of the bars in a metasurface, the plasmonic resonance is excited. On the contrary, when the laser polarization is perpendicular to the main axis of the antennas, the electromagnetic field does not excite the plasmonic resonance, and thus the

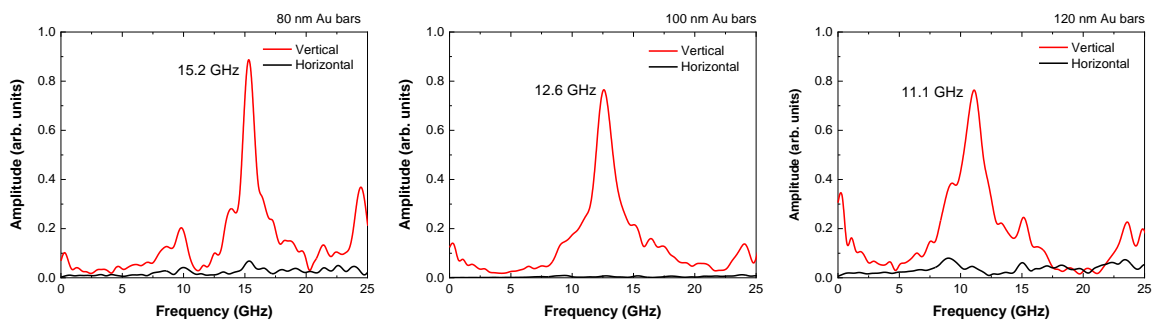


Figure 31: Measured coherent phonon generation spectra using vertical (red curves) and horizontal (black curves) pump-probe polarization in three different control metasurfaces. From left to right: a) Sample formed by an array of 80-nm gold bars oriented in the vertical direction. b) Sample formed by an array of 100-nm gold bars oriented in the vertical direction. c) Sample formed by an array of 120-nm gold bars oriented in the vertical direction.

Figure 31 shows the measured coherent phonon generation spectra using vertical and horizontal pump-probe polarization in the three control metasurfaces. It must be noted that in these experiments, pump and probe beams present the same polarization, and the filtering is performed using color filters. For the generation process, there are two possible extreme situations: i) the laser polarization is perpendicular to the main axis of the antennas, in which case the metasurface is simply transparent, and no coherent phonon generation takes place; and ii) the laser polarization is parallel to the main axis of the antenna, and thus the laser excites the longitudinal plasmonic resonance. The collective oscillation of electrons in the nanoantenna takes a few ps to decay through several scattering processes. These scattering events transform kinetic energy into heat. The rapid heating of the antennas induces a fast dilation (expansion), establishing the origin in time of the coherent acoustic phonons. These acoustic phonons change the size and shape of the antenna, as well as the dielectric function of the metal. In both cases, the variations take place with the frequency of the generated acoustic phonons.

A handwaving argument to explain the optical-properties modification induced by the acoustic phonons is to consider that on the one hand, the phonons change the length of the antenna while inducing an expansion and a reduction of the electron density (constant number of electrons in a bigger volume). An increase in the length of the antenna, or similarly a decrease in the electronic density, induces a red-shift of the plasmon resonance, and therefore a change in the optical reflectivity and transmission.

Let us now consider the detection process. If the probe laser polarization is perpendicular to the main axis of the antennas, then the metasurface is practically transparent, and the presence of phonons or the antennas does not change the optical transmission through the substrate. If the probe laser polarization is parallel to the main axis of the antennas, then the longitudinal plasmon mode is excited, evidencing the plasmonic resonance in transmission. At this point, it is essential to note that the excitation-decay of the plasmon is much shorter than the period of the studied acoustic phonons. In this way, the probe pulse couples to the instantaneous plasmonic mode, which is dynamically modulated by the phonons. So, to detect the coherent acoustic phonons in the metasurface, it is essential that: 1) the probe beam couples to a plasmonic mode and 2) the phonons modulate this plasmonic mode. The high acoustic-impedance mismatch between the gold and the glass substrate justifies the relatively long lifetimes observed.

We designed two metasurfaces to act as polarization-sensitive phonon-transducers. Each metasurface consists of two arrays of parallel bars. The bars of one array are perpendicular to the bars of the other array, as illustrated in Figure 32. Each orientation has an associated optical resonance at a fixed polarization.

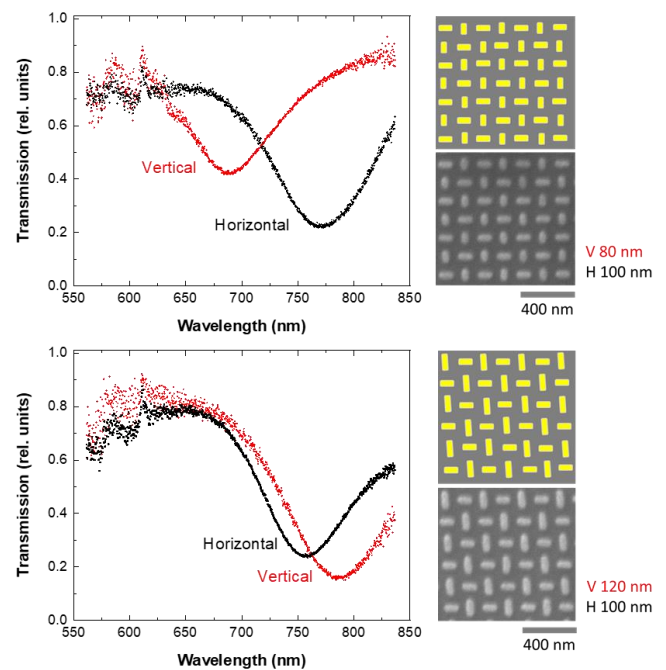
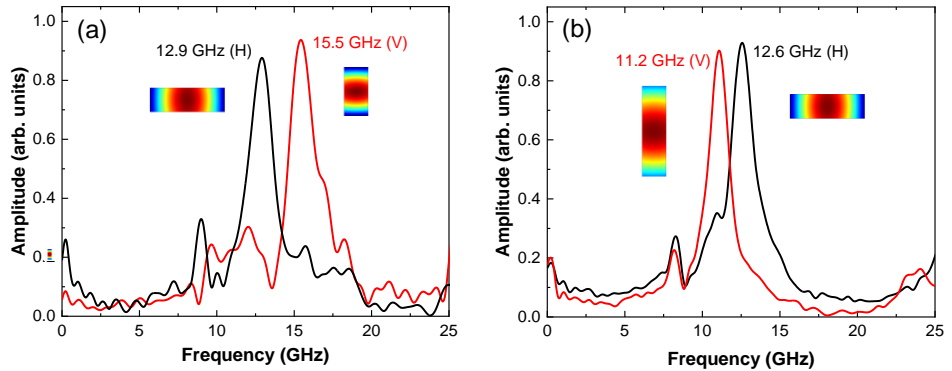


Figure 32: (left) Measured optical transmission of the two studied crossed-bars metasurfaces. The transmission for the vertical (horizontal) polarization is plotted in red (black). (right) Schematics of the studied plasmonic samples and scanning electron micrographies of the metasurfaces. (top) correspond to the crossed-bars metasurface with 80 and 100 nm length bars; (bottom) correspond to crossed-bars metasurface with 100- and 120-nm-length bars, respectively.

In Figure 33, we show the pump-probe measured spectra for different linear polarizations. Figure 33(a) corresponds to the metasurface with 80 and 100 nm length bars, while Figure 33(b) corresponds to the metasurface with 100- and 120-nm-length bars. Each of the four shown spectra presents a clear peak.

In Figure 33(a), the principal peak is located at 12.9 and 15.5 GHz for the horizontal and vertical polarizations, respectively. As in the case of the optical resonances, longer bars (100 nm) present lower frequencies. Similarly, the shorter bars (80 nm) have shorter wavelength eigenmodes. To couple efficiently the incident laser beams (pump and probe) with the plasmonic mode, its polarization has to be parallel to the main axis of the bars. In this way, each array of bars acts as a polarization-sensitive transducer.

Figure 33: Measured coherent phonon generation spectra using vertical (V) and horizontal (H) pump-probe polarization in two different metasurface samples. a) Sample formed by an array of 100-nm gold bars oriented in the horizontal direction and 80-nm gold bars oriented in the vertical direction. b) Sample formed by an array of 120-nm gold bars oriented in the vertical direction and 100-nm gold bars oriented in the horizontal direction.



In Figure 33(b), we show the results corresponding to sample B. In this case, the shorter bars (100 nm) are in the horizontal orientation, and the longer bars (120 nm) are vertically oriented. The vertical (horizontal) polarized pump-probe experiments originate spectra with the main acoustic-phonon peak at 11.2 GHz (12.6 GHz). These measurements confirm that metasurfaces can be used to generate polarization-sensitive phonon transducers.

5.6 Acousto-plasmonic interferences

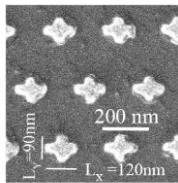


Figure 34: Scanning electron micrographies of the 120 × 90 nm Swiss-cross nanostructure metasurface.

The metasurface shown in Figure 34 consists of an array of Swiss crosses. The shortest (longest) arm of each cross is 90 nm (120 nm). The optical behavior of this metasurface is quite similar to the one of the crossed bars studied in the previous section. Each one of the main axes determines a main longitudinal plasmonic mode. As a first approximation, the presence of the horizontal arm does not affect the resonance of the vertical arm and vice-

versa. This kind of structure had been extensively studied in plasmonics and provides a direct way to encode information with polarization.¹⁸⁸ When one of these plasmonic modes is excited, the electrons move coherently along the excitation axis, and there is no charge movement in the perpendicular direction. In a nutshell, the optical behavior can be modeled as two perpendicular and independent plasmonic resonators.

In the case of the elastic modes, the system cannot be modeled as two perpendicularly polarized independent resonators, as in the case of the plasmonic modes. The main difference arises from the Poisson ratio, linking displacements in different directions. Considering the Poisson ratio and the boundary conditions, we can define two acoustic eigenmodes that we indicate as symmetric and anti-symmetric. The symmetric mode is associated with an isotropic expansion of the Swiss-cross structure. The anti-symmetric mode, on the contrary, has associated an expansion in one direction and a contraction in the perpendicular direction. Both displacement profiles can be observed in Figure 35 (b-c).

Let us consider the coherent generation process again, but this time considering that the plasmonic structures have two different resonances. For the sake of simplicity, let us assume that the pump is vertical. The pump excites then the vertical longitudinal plasmonic mode, and the electrons rapidly dephase on a 5 to 20 fs timescale. The electrons then diffuse throughout the nanostructure at the Fermi velocity, distributing their kinetic energy over the full nanostructure (~ 100 nm of mean free path) within 100 fs. At this point, it is essential to note that the energy is released in the whole structure, and not only over the plasmon spatial profile. The electrons transfer the energy to the lattice resulting in a thermal expansion of the structures that sets off the coherent acoustic phonons. It is evident that following this reasoning, there is no difference between the two experiments using different pump polarizations, except for the efficiency of the process.^{39,174}

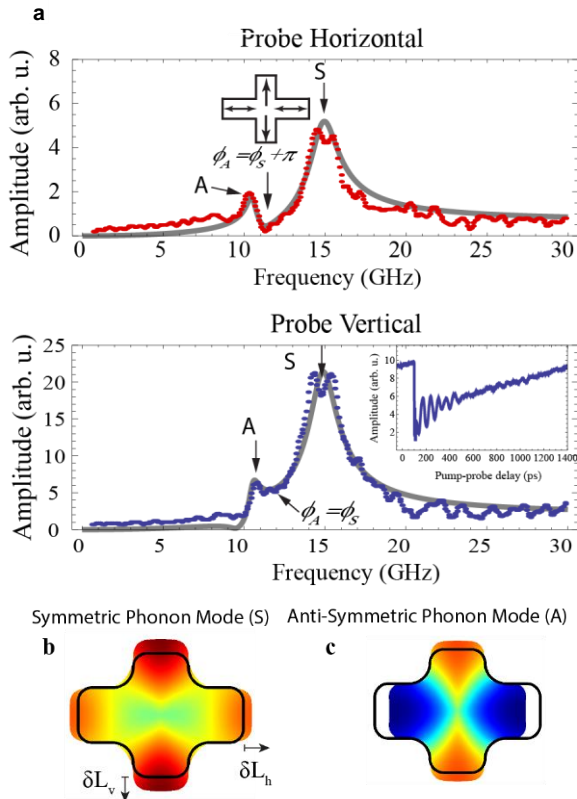


Figure 35: The Fourier transform of the transient transmission for a (a-top) horizontally polarized probe and a (a-bottom) vertically polarized probe. The interference effect at 11 GHz in the transient transmission spectrum for a horizontally polarized probe pulse (top) originates from the two phonon modes changing the optical transmission with equal magnitude and opposite signs, resulting in a zero signal in the differential transmission. When the probe polarization is vertical (a-bottom), the two phonon modes affect the transmission with the same sign, resulting in a constructive contribution. The grey curves are fits with two phonon modes of varying sign. The 120×90 nm Swiss-cross nanostructures (a) support two mechanical eigenmodes, the symmetric eigenmode (b), in which the two arms oscillate in phase, and the antisymmetric (c), where the two arms oscillate out of phase. (b,c) are simulated mechanical displacement profiles at the eigenfrequencies. The superposition between the modes dictates the mechanical dynamics, whose phase and amplitude can be detected with localized surface plasmon polaritons. Each probe plasmon polarization yields a projection of the dynamics, allowing us to sense the mechanical displacement along each axis. The phonon strains the nanostructure, causing geometry and refractive index changes, which in turn modulate the plasmonic resonance, allowing the phonon to be detected through transient optical transmission spectroscopy.

The situation radically changes for the detection process. In this case, the probe couples to a longitudinal mode, and thus it is sensitive to variations of the structure changing this particular resonance. In other words, the spatial selectivity for detecting coherent acoustic phonons is determined by the spatial distribution of the probe plasmon. It does not depend on the electron diffusion length of the constituting materials because of the short lifetime of the probe surface plasmons. The probe plasmon can resolve strain distributions at length scales below the superdiffusion length.

Figure 35 shows the signals measured with different polarizations of the probe. We can observe two clear and well-defined peaks, which correspond to the previously introduced symmetric (~ 15 GHz) and antisymmetric (~ 11 GHz) modes. The intensity of the antisymmetric mode is half the intensity of the symmetric mode, and it is mainly due to the overlap of the mode profiles and the isotropic distribution of energy by the electrons.

When the probe polarization is horizontal, there is an apparent dip at 11.3 GHz. When the probe polarization is vertical, at this frequency, we observe a shoulder connecting both peaks. To understand the measured signals at ~ 11 GHz, it is essential to look at the displacement profiles of the two eigenmodes. For the horizontal arm, the displacement corresponding to the two eigenmodes presents opposite phases, i.e., there is a destructive interference. In the vertical arm, on the contrary, both displacement profiles contribute in phase to the change in transmission, i.e., there is a constructive interference. The unique

characteristic of the plasmonic structures of polarization-sensitive resonances allowed us to sense strain distributions in the deep subwavelength regime, localized in parts of the studied nanostructures.

5.7 Discussion and conclusions

We extended the concept of colocalization of light and sound to 3D micropillars both theoretically and experimentally. By laterally etching a planar structure, optophononic micropillars can be fabricated. In these structures, the contrast in the indices of refraction of the air and the semiconductor induces lateral confinement for the light; and the contrast in the acoustic impedances is at the origin of the lateral confinement of vibrations. The same GaAs/AlAs micropillars can host single quantum dots, accelerating the emission of single photons, and constituting the brightest single-photon sources.⁶⁰ It is possible to integrate quantum wells, extending the possibility of engineering the acoustic phonons to polaritonic systems.¹³¹

GaAs/AlAs pillar microcavities constitute new optomechanical resonators performing in the unprecedented 18-100 GHz mechanical frequency range, showing highly-promising features such as state-of-the-art quality factor-frequency products.¹⁸⁰ We showed that gluing optophononic semiconductor cavities to a single-mode fiber lifts the need for focusing optics to excite and detect coherent acoustic phonons. The mode matching achieved in our samples allowed us to observe stable signals over at least a full day and coherent phonon signals at extremely low excitation powers of $1\mu\text{W}$. The monolithic sample structure is transportable, making it a potential means to perform reproducible plug-and-play pump-probe experiments in individual microstructures.⁷⁵ The integration with fibers might establish the missing link between high-frequency acoustic phonon engineering^{1,27,189-191} and stimulated Brillouin scattering in structured optical fibers¹⁹²⁻¹⁹⁶.

Over the last years, remarkable results in the control of acoustic phonons in single antennas or even in the transfer of signals between individual resonators have been achieved.^{17,37,176} The use of metasurfaces could take full advantage of this individual resonator optimization to explore advanced transduction functionalities. We showed how a metasurface could be used as a tailorable transducer to generate and detect high-frequency acoustic phonons.¹⁷⁴ In particular, we have explored crossed bars systems in which the bars are part of the same structure (Swiss-cross), or the bars are spatially separated. Both cases present very similar optical behavior; however, the elastic eigenmodes are dramatically different. When the two bars are separated, the eigenmodes can be easily described as the longitudinal modes of a bar, and the laser polarization acts simply as a selective excitation (and detection) tool. The elastic eigenmodes of the Swiss-crosses, on the contrary, are described as linear combinations of the modes of the forming bars. We can classify the two eigenmodes as symmetric when the two bars are expanding or contracting in-phase and antisymmetric when the bars are oscillating in counter phase. The fact that the plasmonic modes and the elastic modes do not present the same spatial profile enables the possibility of measuring and resolving strain distributions in the deep subwavelength regime.⁴

All these results constitute just the first steps in the field of acoustoplasmonics. The manipulation of optical fields to control the transduction of acoustic phonons, as well as the engineering of complex acoustoplasmonic structures with novel functionalities, are just two exciting perspectives of the field. The possibility of including active optical materials in plasmonic metasurfaces or even exploring quantum phenomena are two promising research lines showing their first results. These new research fields can be revisited, incorporating ultrafast vibrations as a completely new design knob. The use of more complex structures showing multiple acoustic and plasmonic modes, or taking advantage of chirality for both light and sound constitute the starting points of a new field.

Contributions related to this chapter

Design, optimization, and experimental demonstration of a novel optomechanical platform based on semiconductor micropillars. Micropillars work at record-high frequencies of 20 GHz, one order of

magnitude higher than the best previously reported system, and present a record high value for the mechanical $Q \times f$ indicator. Integration of ultrahigh-frequency resonators into a fibered platform. Theoretical proposal and experimental development of a new platform to couple light and sound based on acoustoplasmonic metasurfaces. Design of an acoustoplasmonic metasurface to generate tunable coherent acoustic phonons. Experimental demonstration of optical interference effects between signals generated by phononic modes in a nanostructure. Spatial strain probing in the deep subwavelength regime.

- A. *Ultrafast Acousto-Plasmonic Control and Sensing in Complex Nanostructures*
K. O'Brien*, [N. D. Lanzillotti-Kimura*](#), J. Rho, H. Suchowski, X. Yin, and X. Zhang
Nat. Commun. **5**, 4042 (2014).
- B. *Micropillar Resonators for Optomechanics in the Extremely High 19–95-GHz Frequency Range*
S. Anguiano, A. E. Bruchhausen, B. Jusserand, I. Favero, F. R. Lamberti, L. Lanco, I. Sagnes, A. Lemaître, [N. D. Lanzillotti-Kimura](#), P. Senellart, and A. Fainstein
Phys. Rev. Lett. **118**, 263901 (2017)
- C. *Optomechanical Properties of GaAs/AlAs Micropillar Resonators Operating in the 18 GHz Range*
F. R. Lamberti, Q. Yao, L. Lanco, D. T. Nguyen, M. Esmann, A. Fainstein, P. Sesin, S. Anguiano, V. Villafañe, A. Bruchhausen, P. Senellart, I. Favero, and [N. D. Lanzillotti-Kimura](#)
Opt. Express **25**, 24437 (2017)
- D. *Polarization-Controlled Coherent Phonon Generation in Acoustoplasmonic Metasurfaces*
[N. D. Lanzillotti-Kimura](#), K. P. O'Brien, J. Rho, H. Suchowski, X. Yin, and X. Zhang
Phys. Rev. B **97**, 235403 (2018)
- E. *Scaling Rules in Optomechanical Semiconductor Micropillars*
S. Anguiano, P. Sesin, A. E. Bruchhausen, F. R. Lamberti, I. Favero, M. Esmann, I. Sagnes, A. Lemaître, [N. D. Lanzillotti-Kimura](#), P. Senellart, and A. Fainstein
Phys. Rev. A **98**, 063810 (2018)
- F. *Optical Cavity Mode Dynamics and Coherent Phonon Generation in High-Q Micropillar Resonators*
S. Anguiano, A. E. Bruchhausen, I. Favero, I. Sagnes, A. Lemaître, [N. D. Lanzillotti-Kimura](#), and A. Fainstein
Phys. Rev. A **98**, 013816 (2018)
- G. *Brillouin Scattering in Hybrid Optophononic Bragg Micropillar Resonators at 300 GHz*
M. Esmann, F. R. Lamberti, A. Harouri, L. Lanco, I. Sagnes, I. Favero, G. Aubin, C. Gomez-Carbonell, A. Lemaître, O. Krebs, P. Senellart, and [N. D. Lanzillotti-Kimura](#)
Optica **6**, 854 (2019)
- H. *Fiber-Integrated Microcavities for Efficient Generation of Coherent Acoustic Phonons*
O. Ortiz, F. Pastier, A. Rodriguez, Priya, A. Lemaitre, C. Gomez-Carbonell, I. Sagnes, A. Harouri, P. Senellart, V. Giesz, M. Esmann, and [N. D. Lanzillotti-Kimura](#)
Appl. Phys. Lett. **117**, 183102 (2020)

Chapter 6

Research perspectives

In the previous chapters, a series of optophononic devices was presented, where the confinement and propagation characteristics were optimized. The engineering of the transduction mechanisms was detailed, and novel measurement protocols were developed. In all cases, the physics governing the phonon engineering aspects was based on classical wave dynamics and, in general, linear processes.

In the next sections, I present three open directions of what I believe might be game-changers in the future of nanophononics and nanomechanics. First, I present a few concepts to study coherence properties and control the propagation in complex three-dimensional geometries. The second research line is devoted to two strategies to achieve reconfigurable optophononic devices. And finally, I propose the development of quantum nanoacoustic devices.

6.1 Integrated phonon networks: confinement and propagation

During the past 10 years, fine control on the dynamics of high-frequency acoustic phonons in planar structures has been achieved.^{2,12,73,110,126,127,130,197–199} However, the 3D control of their propagation remains a vast and almost unexplored research field. In this research line, I propose to engineer and develop the elements at the core of an integrated nanophononic network, focusing on the design and demonstration of acoustic phonon waveguides able to couple different subsystems. The experimental demonstration will rely mainly on the coherent generation and detection of acoustic phonons using ultrafast lasers. The concept at the heart of our phonon resonators and waveguides is the DBR-based acoustic cavity made of GaAs/AIAs.

In the fields of photonics, as well as polaritonics, light confinement and propagation have been controlled at will in optical structures^{78,159,160} highly similar to the ones envisioned here, allowing the study of phenomena otherwise unreachable. Waveguides are fundamental optics elements that facilitate the interconnection of different optical subsystems and information processing. We plan to transfer some of these concepts into the field of nanophononics.

In the fields of optomechanics and surface acoustic waves, acoustic waveguides have been proposed with typical frequencies in the MHz regime, reaching a few GHz at most. These results represent an unexplored and inspiring set of challenges in the physics of ultrahigh-frequency acoustic phonons that we intend to address in this research line. One of the objectives is to develop waveguides that allow us to measure the transport of acoustic phonons with frequencies around 20 GHz. We plan to demonstrate complex localization phenomena like Bloch oscillations and topological localization in 2D systems and determine important transport characteristics such as coherence lengths and mean free paths of the propagating phonons.

It is known that the dynamics of light can be tailored by coupling optical microcavities in double and multiple cavity devices. Based on these concepts, we will study how coupled acoustic nanocavities based on micropillars could also be used to control the propagation and dynamics of phonons, including the generation of effective acoustic potentials, simulating an effective force on propagating vibrations. An extension of these concepts into full bidimensional networks and waveguides constitutes the long-term objective of this research line.

The development of a phonon network is organized around three objectives, described below.

6.1.1 Observation of coupled acoustic modes in a 3D phononic molecule

By coupling two micropillars, we can form an optical molecule. The coupling in the optophononic molecule will be studied by changing the separation between the centers of the two optophononic micropillars, individually changing the diameter, and by changing the etching conditions to increase the coupling. Once the elastic coupling conditions between two micropillars have been established, a solid physical bridge will be extended between the two separated structures. This bridge will be optimized to act as a waveguide or transmission line for the acoustic phonons that were initially confined in the micropillars. The experimental strategy will consist of focusing the pump beam onto one of the micropillars and the probe beam onto the second one, both spots being spatially separated. The observation of a beating in the time-dependent optical reflectivity and the presence of two peaks in the spectral domain are the main indicators of the success of this objective.

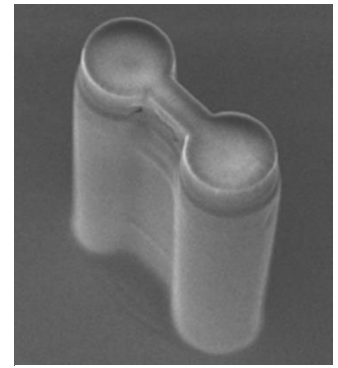


Figure 36: SEM image of two micropillars connected by a phononic waveguide.

6.1.2 Measurement of high-frequency acoustic Bloch oscillations and topological states

By scaling up the complexity of our devices, we intend to demonstrate complex localization phenomena such as Bloch oscillations of GHz acoustic phonons and topologically protected states in bidimensional micropillar networks. The coupling of multiple identical micropillars induces a periodic acoustic potential, which leads to the formation of acoustic bands. In addition, by gradually changing the radius of each micropillar (or equivalently the thickness of the layers), it is possible to generate an effective linear potential equivalent to an applied electric field for electrons. By individually engineering the couplings between micropillars, it is also possible to engineer the topological phases of the structure, build an artificial phononic graphene, and control the propagation properties in bidimensional networks.

6.1.3 Design and optimization of phonon interferometers

Another essential feature that we will pursue related to on-chip phonon wave manipulation is the implementation of acoustic-phonon beam splitters consisting, for instance, in the bifurcation of an acoustic waveguide. High-frequency acoustic phonons might provide a platform for developing novel acoustic functionalities and even quantum simulators. In the prospect of propagating the information using acoustic waves, we will evaluate the one or two phonon coherence using on-chip phonon interferometers. We will develop compact Sagnac and Mach-Zehnder interferometers for acoustic phonons that can be externally actuated through strain or heat. Playing on the length of the interferometer will allow us to evaluate the coherence length of the propagating acoustic waves. These devices will be designed for high-frequency phonons to work near the single phonon regime at 4K and with the long-term objective of developing the platform for future quantum nanophononic applications.

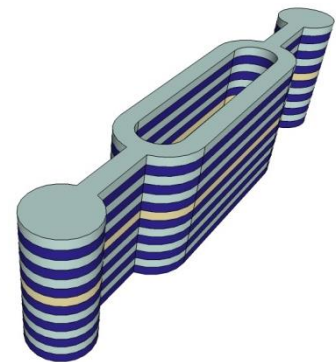


Figure 37: Schematics of two micropillars connected by a phononic Mach-Zehnder interferometer.

The described structures are similar to those used to fabricate VCSEL devices, polariton microcavities, and ridge waveguides. Adding control of the phonon environment in these devices will open the road to a wide variety of phenomena as well as future innovative functionalities.

6.2 Reconfigurable optophononic devices

Phononic crystals and acoustic metamaterials enabled the study of novel physical phenomena and new applications. The functionalization and dynamical tuning of artificial acoustic materials, particularly at the

nanoscale, would be a breakthrough in the engineering of intelligent and programmable materials. In nanoacoustics, despite the potential impact in the development of non-destructive testing techniques, optoelectronics, and in general in fundamental physics, no tunable nanophononic devices have been reported up to now. In this research line, we will explore two paths: i) mesoporous materials and ii) VO₂, phase changing materials (PCMs), and ITO.

6.2.1 Mesoporous materials for nanophononic applications

Most of the nanophononic applications are based on already developed semiconductor technology. However, a full variety of materials remains unexplored in nanophononics, and colloidal crystals or polymer multilayers seem promising towards new developments in phononic crystals or metamaterials.¹ For example, hypersonic one-dimensional crystals were made up of alternating layers of poly(methyl methacrylate) and porous silica.²⁰⁰ More recently, a new class of tunable hypersonic phononic crystals has been developed based on economically viable polymer-tethered colloids that present a tunable hybridization gap.⁶ These systems opened the path toward the integration of soft matter-derived materials. A further step in complexity could be attained by building phononic devices with responsive nanomaterials, which appear as a potential gamechanger in the fields of nanoacoustics and nanophononics.

In the last years, the development of stimuli-responsive materials capable of transducing external stimuli into mechanical and physical changes has become a blooming field.²⁰¹ In particular, mesoporous materials present high interest and potential to add responsiveness to thin-film technology. Mesoporous thin films, produced by combining sol-gel synthesis with self-assembly, can be designed in order to selectively condense external vapors or act as perm-selective membranes. The variation of optical and mechanical properties after adsorption and permeation phenomena endows these systems to be naturally responsive to the environment.²⁰² Mesoporous photonic crystals with a selective optical response to vapors, or molecular size are an excellent example that molecular, supramolecular, or photonic information can be encoded into the structure of a multilayer at several length scales, and indeed combined with a plasmonic response.²⁰³ The combination of semiconductor and mesoporous systems opens up a new path for the design of intelligent, programmable nanoacoustic matter.^{204,205}

The mesoporous layers cited above can be readily integrated on top or even within these superlattices as responsive modules that can modify the mechanical behavior of the whole device when exposed to a given stimulus. Intending to design and develop more complex devices, we have recently demonstrated that mesoporous SiO₂ and TiO₂ thin films can act as the resonant layer of acoustic nanocavities.³

6.2.2 Indium-Tin-Oxide, vanadium dioxide, and other PCMs

A radically different path to achieve tunability and reconfigurability is the use of materials showing a controllable and reversible change in the optical or acoustic properties such as vanadium dioxide (VO₂)²⁰⁶ or Transparent Conductive Oxides like Indium-Tin-Oxide (ITO). Recent developments in optics using PCMs^{207–209} show an interesting and promising roadmap for nanophononics, where most of the technological developments can be directly mapped into nanoacoustic applications.

At temperatures less than 67° C, VO₂ has a monoclinic crystal structure. When heated to more than 67° C, it transitions to a tetragonal structure. At the same temperature, crystalline VO₂ converts from an electrical insulator to a conductor. The same transition can be induced by applying an external voltage to a thin film of VO₂. The monoclinic and tetragonal structures have associated different speeds of sound. This change in the elastic properties makes it an ideal material to design tunable nanoacoustic devices. The first step would be to revisit the simplest acoustic devices presented in Chap. 2, and then expand the set of materials compatible with the VO₂. A layer of VO₂ could act like the active part of the system, able to dynamically change the eigenstates of a Fabry-Perot resonator. In this case, the transition that takes place in the scale of picoseconds could also be the platform for the study of time-dependent nanophononic structures.

ITO belongs to the class of transparent conducting oxides, which can be doped depending on the oxygen vacancy and interstitial metal dopant concentrations.²¹⁰ Furthermore, the carrier density can be significantly increased when ITO becomes part of a MOS-capacitor design upon applying an electrical bias due to the formation of an accumulation layer.^{167,211} Thus, an ITO layer could be integrated into tunable nanophononic transducers, also based on the structures presented in Chapter 2.

6.3 Quantum nanoacoustics

The high frequencies of the acoustic phonons have associated small occupation numbers, enabling the operation of the proposed devices in the quantum regime. For instance, the possibility of having low phonon-number in particularly engineered discrete modes opens the possibility to explore novel phonon-exchange protocols and quantum interfaces.

In this research line, I intend to explore two objectives. Firstly, the coherent exchange of single-phonons between two photonic states in correlated Raman processes, and secondly, the interfacing of an acoustic mode with a quantum emitter, in our particular case, with a semiconductor quantum dot.

6.3.1 Acoustic-phonon exchange

The objective is to develop (theoretically and experimentally) the protocol for the non-classical generation of phonons in a hybrid micropillar resonator. Recent works reported the use of optical phonons for the generation of non-classical correlations.^{212–216} By using an optophononic cavity, we add the possibility of gaining full control over the acoustic excitations, and thus over the interaction process.

We will set up a versatile experimental method wherein one short laser pulse generates non-classically correlated Stokes and anti-Stokes photons. In Figure 38, we show the principle of the proposed experiment where a pump pulse induces the generation of a phonon (Stokes process), while the probe pulse absorbs the same phonon (anti-Stokes process).

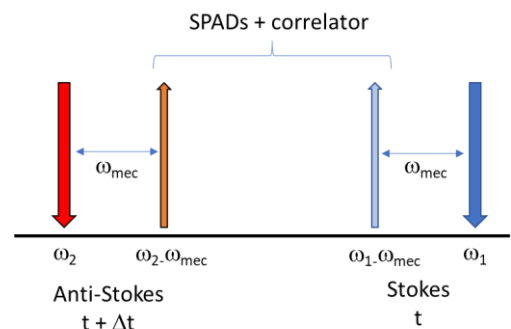


Figure 38: Schematics of the correlation of Stokes and anti-Stokes photon pairs in an acoustic resonator. ω_{mec} , ω_1 and ω_2 indicate the frequencies of the acoustic resonance and the two lasers.

The coincidences of the Stokes and anti-Stokes photon signals will be recorded by the single-photon detectors connected to a correlation unit. The measured value of the second-order intensity cross-correlation function at zero delays will be used to authenticate the non-classical relation of the Stokes and anti-Stokes photon via the exchange of a single phonon. In this case, the Brillouin cross-correlation experiments will allow us to study the dynamics of a single phonon created as a consequence of a pump laser pulse, which subsequently produces an anti-Stokes photon with the delayed probe laser pulse.

By manipulating the wavelength of the lasers, the time delay between the pulses, and the coupling conditions with the different resonances in an optophononic micropillar, we target the full engineering of the interaction process. Different regimes will be explored, like the interaction of photons with single and multiple phonons will be investigated.

6.3.2 Acoustic cavity quantum electrodynamics

This research objective will be carried out in collaboration with the team of Prof. Pascale Senellart. Quantum dots are one of the most promising semiconductor quantum bits, with many demonstrations of quantum functionalities in the last decade. When optically excited, a single exciton in a QD (X) emits single photons at a well-defined discrete energy. Yet, QDs are coupled to the vibrational modes of the crystal they are embedded in, limiting the coherence of the quantum states. An exciting and open challenge made possible by the recent progress in nanophononics is to engineer the interaction between phonons and a single quantum emitter. We aim at demonstrating acoustic cavity quantum electrodynamics phenomena

with single QDs. By precisely positioning a single QD in an acoustic cavity, we ambition to enhance the emission of phonons with a well-defined frequency and spatial mode. We will use the unique technology developed at the C2N to precisely position a single QD in an acoustic cavity. The technique allows us to achieve a deterministic coupling of a QD with an optical microcavity. By the same token, it will be possible to deterministically couple a QD to a single-mode nanomechanical resonator, taking into account the design principles discussed in Chapters 4 and 5. Up to now, none of the active groups in QDs-CQED and nanophononics has attempted to engineer the phononic environment (at 10's of GHz frequencies) of a single quantum dot to control the quantum emitter properties. One of the major roadblocks in the development of a network-based on QDs is their dispersion in size and thus in the X energy. The ability of the acoustic phonons to couple to excitons regardless of their energy is a solution that has not been explored yet to propagate quantum information. Such possibility has only been proposed in the context of optomechanics, with first results with the use of surface acoustic waves and superconducting qubits. During the following years, I plan to develop the first building blocks of such a phonon-bus for optically active solid-state quantum bits.

The objective is to demonstrate for the very first time the engineering of the phonon density of states around a single QD so as to make the phonon coupling a tool for future quantum applications. We will measure the modification of the phonon density of states through the investigation of the phonon-assisted emission of a single QD coupled to an acoustic micropillar cavity, i.e., the spontaneous emission and absorption of acoustic phonons. While the zero-phonon line of a QD emission is a few μeV wide, the bulk phonon-assisted emission spreads on a few meV, resulting in a very low signal at a given energy. By varying the acoustic cavity parameters (geometry, materials, thickness), we aim at demonstrating the phonon Purcell effect, manifesting itself by an enhanced phonon emission at the acoustic cavity energy. Note that the optical cavity will be used here to strongly enhance the phonon-assisted emission, as it was recently demonstrated.

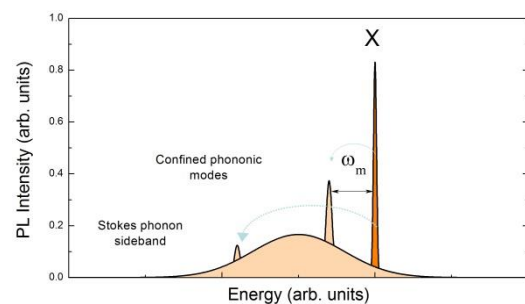


Figure 39: Schematic indicating the Stokes emission related to an exciton (X) assisted by confined acoustic phonons of energy ω_m .

The demonstration of the phononic Purcell effect would constitute the first building block towards the conception of more complex devices. For instance, we will aim at demonstrating an acoustic phonon exchange between two single quantum dots. The objective would be to probe the induced change in the acoustic-phonon population by a first QD in a resonator by measuring the phonon sidebands of a second QD emission. Such observation would be the first evidence of the coupling of two electronic states mediated by the same ultrahigh-frequency phonon confined mode.

By bridging the gaps with other research fields such as optomechanics, plasmonics, polaritonics, and quantum technologies, I am confident that nanophononics has great potential to unlock new paths in the engineering of nanodevices and unveil a plethora of novel and exciting physical phenomena.

Bibliography

- ¹ S. Volz, J. Ordonez-Miranda, A. Shchepetov, M. Prunnila, J. Ahopelto, T. Pezeril, G. Vaudel, V. Gusev, P. Ruello, E.M. Weig, M. Schubert, M. Hettich, M. Grossman, T. Dekorsy, F. Alzina, B. Graczykowski, E. Chavez-Angel, J. Sebastian Reparaz, M.R. Wagner, C.M. Sotomayor-Torres, S. Xiong, S. Neogi, and D. Donadio, *Eur. Phys. J. B* **89**, 15 (2016).
- ² A. Huynh, N.D. Lanzillotti-Kimura, B. Jusserand, B. Perrin, A. Fainstein, M.F. Pascual-Winter, E. Peronne, and A. Lemaître, *Phys. Rev. Lett.* **97**, 115502 (2006).
- ³ N.L. Abdala, M. Esmann, M.C. Fuertes, P.C. Angelomé, O. Ortiz, A. Bruchhausen, H. Pastoriza, B. Perrin, G.J.A.A. Soler-Illia, and N.D. Lanzillotti-Kimura, *J. Phys. Chem. C* **124**, 17165 (2020).
- ⁴ K. O'Brien, N.D. Lanzillotti-Kimura, J. Rho, H. Suchowski, X. Yin, and X. Zhang, *Nat. Commun.* **5**, 4042 (2014).
- ⁵ P.M. Walker, J.S. Sharp, A.V. Akimov, and A.J. Kent, *Appl. Phys. Lett.* **97**, 073106 (2010).
- ⁶ E. Alonso-Redondo, M. Schmitt, Z. Urbach, C.M. Hui, R. Sainidou, P. Rembert, K. Matyjaszewski, M.R. Bockstaller, and G. Fytas, *Nat. Commun.* **6**, 8309 (2015).
- ⁷ M. Trigo, A. Bruchhausen, A. Fainstein, B. Jusserand, and V. Thierry-Mieg, *Phys. Rev. Lett.* **89**, 227402 (2002).
- ⁸ M. Aspelmeyer, T.J. Kippenberg, and F. Marquardt, *Rev. Mod. Phys.* **86**, 1391 (2014).
- ⁹ L. Ding, C. Baker, P. Senellart, A. Lemaître, S. Ducci, G. Leo, and I. Favero, *Appl. Phys. Lett.* **98**, 113108 (2011).
- ¹⁰ T.J. Kippenberg and K.J. Vahala, *Science* **321**, 1172 (2008).
- ¹¹ M. Eichenfield, J. Chan, R.M. Camacho, K.J. Vahala, and O. Painter, *Nature* **462**, 78 (2009).
- ¹² A. Fainstein, N.D. Lanzillotti-Kimura, B. Jusserand, and B. Perrin, *Phys. Rev. Lett.* **110**, 037403 (2013).
- ¹³ J. Chan, M. Eichenfield, R. Camacho, and O. Painter, *Opt. Express* **17**, 3802 (2009).
- ¹⁴ M. Eichenfield, R. Camacho, J. Chan, K.J. Vahala, and O. Painter, *Nature* **459**, 550 (2009).
- ¹⁵ G. Bahl, K.H. Kim, W. Lee, J. Liu, X. Fan, and T. Carmon, *Nat. Commun.* **4**, 1994 (2013).
- ¹⁶ R. Dahan, L.L. Martin, and T. Carmon, *Optica* **3**, 175 (2016).
- ¹⁷ F. Della Picca, R. Berte, M. Rahmani, P. Albella, J.M. Bujjamer, M. Poblet, E. Cortés, S.A. Maier, and A.V. Bragas, *Nano Lett.* **16**, 1428 (2016).
- ¹⁸ M.D. LaHaye, J. Suh, P.M. Echternach, K.C. Schwab, and M.L. Roukes, *Nature* **459**, 960 (2009).
- ¹⁹ J.-M. Pirkkalainen, S.U. Cho, J. Li, G.S. Paraoanu, P.J. Hakonen, and M.A. Sillanpää, *Nature* **494**, 211 (2013).
- ²⁰ R.W. Andrews, R.W. Peterson, T.P. Purdy, K. Cicak, R.W. Simmonds, C.A. Regal, and K.W. Lehnert, *Nat. Phys.* **10**, 321 (2014).
- ²¹ M.V. Gustafsson, T. Aref, A.F. Kockum, M.K. Ekström, G. Johansson, and P. Delsing, *Science* **346**, 207 (2014).
- ²² K. Toyoda, R. Hiji, A. Noguchi, and S. Urabe, *Nature* **527**, 74 (2015).
- ²³ E. Yablonovitch, *Phys. Rev. Lett.* **58**, 2059 (1987).
- ²⁴ E. Yablonovitch, *JOSA B* **10**, 283 (1993).
- ²⁵ V. Agarwal, J.A. del Río, G. Malpuech, M. Zamfirescu, A. Kavokin, D. Coquillat, D. Scalbert, M. Vladimirova, and B. Gil, *Phys. Rev. Lett.* **92**, 097401 (2004).
- ²⁶ A. Kavokin, G. Malpuech, A. Di Carlo, P. Lugli, and F. Rossi, *Phys. Rev. B* **61**, 4413 (2000).
- ²⁷ A.A. Balandin, *J. Nanosci. Nanotechnol.* **5**, 1015 (2005).
- ²⁸ N.D. Lanzillotti-Kimura, A. Fainstein, A. Lemaître, and B. Jusserand, *Appl. Phys. Lett.* **88**, 083113 (2006).
- ²⁹ M. Trigo, A. Bruchhausen, A. Fainstein, B. Jusserand, and V. Thierry-Mieg, *Phys. Rev. Lett.* **89**, 227402 (2002).
- ³⁰ A. Huynh, N. Lanzillotti-Kimura, B. Jusserand, B. Perrin, A. Fainstein, M. Pascual-Winter, E. Peronne, and A. Lemaître, *Phys. Rev. Lett.* **97**, 115502 (2006).
- ³¹ N.D. Lanzillotti-Kimura, A. Fainstein, and B. Jusserand, *Ultrasonics* **56**, 80 (2015).
- ³² W. Maryam, A.V. Akimov, R.P. Champion, and A.J. Kent, *Nat. Commun.* **4**, 2184 (2013).

- ³³ N. Lanzillotti-Kimura, A. Fainstein, B. Perrin, B. Jusserand, A. Soukiassian, X. Xi, and D. Schlom, *Phys. Rev. Lett.* **104**, 187402 (2010).
- ³⁴ K. Vahala, M. Herrmann, S. Knünz, V. Batteiger, G. Saathoff, T.W. Hänsch, and T. Udem, *Nat. Phys.* **5**, 682 (2009).
- ³⁵ C.-K. Sun, J.-C. Liang, and X.-Y. Yu, *Phys. Rev. Lett.* **84**, 179 (2000).
- ³⁶ C. Brüggemann, A.V. Akimov, A.V. Scherbakov, M. Bombeck, C. Schneider, S. Höfling, A. Forchel, D.R. Yakovlev, and M. Bayer, *Nat. Photonics* **6**, 30 (2012).
- ³⁷ V. Juvé, A. Crut, P. Maioli, M. Pellarin, M. Broyer, N. Del Fatti, and F. Vallée, *Nano Lett.* **10**, 1853 (2010).
- ³⁸ N. Lanzillotti-Kimura, A. Fainstein, C. Balseiro, and B. Jusserand, *Phys. Rev. B* **75**, 024301 (2007).
- ³⁹ K. O'Brien, N.D. Lanzillotti-Kimura, J. Rho, H. Suchowski, X. Yin, and X. Zhang, *Nat. Commun.* **5**, (2014).
- ⁴⁰ N. Large, L. Saviot, J. Margueritat, J. Gonzalo, C.N. Afonso, A. Arbouet, P. Langot, A. Mlayah, and J. Aizpurua, *Nano Lett.* **9**, 3732 (2009).
- ⁴¹ V.V. Temnov, *Nat. Photonics* **6**, 728 (2012).
- ⁴² A. Fainstein, N.D. Lanzillotti-Kimura, B. Jusserand, and B. Perrin, *Phys. Rev. Lett.* **110**, 037403 (2013).
- ⁴³ V. Laude, J.-C. Beugnot, S. Benchabane, Y. Pennec, B. Djafari-Rouhani, N. Papanikolaou, J.M. Escalante, and A. Martinez, *Opt. Express* **19**, 9690 (2011).
- ⁴⁴ I.E. Psarobas, N. Papanikolaou, N. Stefanou, B. Djafari-Rouhani, B. Bonello, and V. Laude, *Phys. Rev. B* **82**, 174303 (2010).
- ⁴⁵ Q. Rolland, M. Oudich, S. El-Jallal, S. Dupont, Y. Pennec, J. Gazalet, J. Kastelik, G. Leveque, and B. Djafari-Rouhani, *Appl. Phys. Lett.* **101**, 061109 (2012).
- ⁴⁶ A.A. Balandin, *ACS Nano* **14**, 5170 (2020).
- ⁴⁷ A.A. Balandin and D.L. Nika, *Mater. Today* **15**, 266 (2012).
- ⁴⁸ P.V. Huong, R. Cavagnat, P.M. Ajayan, and O. Stephan, *Phys. Rev. B* **51**, 10048 (1995).
- ⁴⁹ V. Narayanamurti, H.L. Störmer, M.A. Chin, A.C. Gossard, and W. Wiegmann, *Phys. Rev. Lett.* **43**, 2012 (1979).
- ⁵⁰ N.D. Lanzillotti-Kimura, A. Fainstein, B. Jusserand, A. Lemaître, O. Mauguin, and L. Largeau, *Phys. Rev. B* **76**, 174301 (2007).
- ⁵¹ N.D. Lanzillotti-Kimura, B. Perrin, A. Fainstein, B. Jusserand, and A. Lemaître, *Appl. Phys. Lett.* **96**, 053101 (2010).
- ⁵² C. Thomsen, H.T. Grahn, H.J. Maris, and J. Tauc, *Phys. Rev. B* **34**, 4129 (1986).
- ⁵³ C. Thomsen, J. Strait, Z. Vardeny, H.J. Maris, J. Tauc, and J.J. Hauser, *Phys. Rev. Lett.* **53**, 989 (1984).
- ⁵⁴ M. De Luca, C. Fasolato, M.A. Verheijen, Y. Ren, M.Y. Swinkels, S. Kölling, E.P.A.M. Bakkers, R. Rurali, X. Cartoixa, and I. Zardo, *Nano Lett.* **19**, 4702 (2019).
- ⁵⁵ O. Ortíz, M. Esmann, and N.D. Lanzillotti-Kimura, *Phys. Rev. B* **100**, 085430 (2019).
- ⁵⁶ N.D. Lanzillotti-Kimura, A. Fainstein, C.A. Balseiro, and B. Jusserand, *Phys. Rev. B* **75**, 024301 (2007).
- ⁵⁷ B. Jusserand and M. Cardona, in *Light Scatt. Solids V* (Springer, Berlin, Heidelberg, 1989), pp. 49–152.
- ⁵⁸ M. Esmann, F.R. Lamberti, P. Senellart, I. Favero, O. Krebs, L. Lanco, C. Gomez Carbonell, A. Lemaître, and N.D. Lanzillotti-Kimura, *Phys. Rev. B* **97**, 155422 (2018).
- ⁵⁹ F.R. Lamberti, M. Esmann, A. Lemaître, C. Gomez Carbonell, O. Krebs, I. Favero, B. Jusserand, P. Senellart, L. Lanco, and N.D. Lanzillotti-Kimura, *Appl. Phys. Lett.* **111**, 173107 (2017).
- ⁶⁰ N. Somaschi, V. Giesz, L.D. Santis, J.C. Loredó, M.P. Almeida, G. Hornecker, S.L. Portalupi, T. Grange, C. Antón, J. Demory, C. Gómez, I. Sagnes, N.D. Lanzillotti-Kimura, A. Lemaître, A. Auffeves, A.G. White, L. Lanco, and P. Senellart, *Nat. Photonics* **10**, (2016).
- ⁶¹ D. Bajoni, P. Senellart, E. Wertz, I. Sagnes, A. Miard, A. Lemaître, and J. Bloch, *Phys. Rev. Lett.* **100**, 047401 (2008).
- ⁶² J.-Gerard and B. Gayral, *J. Light. Technol.* **17**, 2089 (1999).
- ⁶³ G. Rozas, M.F.P. Winter, B. Jusserand, A. Fainstein, B. Perrin, E. Semenova, and A. Lemaître, *Phys. Rev. Lett.* **102**, 015502 (2009).
- ⁶⁴ M. Cardona and M.H. Brodsky, editors, *Light Scattering in Solids*, 2nd corr. and updated ed (Springer-Verlag, Berlin ; New York, 1983).
- ⁶⁵ A. Fainstein and B. Jusserand, in *Light Scatt. Solid IX* (Springer, Berlin, Heidelberg, 2006), pp. 17–110.
- ⁶⁶ A. Fainstein, B. Jusserand, and V. Thierry-Mieg, *Phys. Rev. B* **53**, R13287 (1996).

- ⁶⁷ A. Fainstein, B. Jusserand, and V. Thierry-Mieg, *Phys. Rev. Lett.* **75**, 3764 (1995).
- ⁶⁸ A. Fainstein and B. Jusserand, *Phys. Rev. B* **57**, 2402 (1998).
- ⁶⁹ N.D. Lanzillotti-Kimura, A. Fainstein, B. Jusserand, and A. Lemaître, *Phys. Rev. B* **79**, 035404 (2009).
- ⁷⁰ P. Lacharmoise, A. Fainstein, B. Jusserand, and V. Thierry-Mieg, *Appl. Phys. Lett.* **84**, 3274 (2004).
- ⁷¹ N.D. Lanzillotti-Kimura, A. Fainstein, B. Perrin, and B. Jusserand, *Phys. Rev. B* **84**, 064307 (2011).
- ⁷² P. Ruello and V.E. Gusev, *Ultrasonics* **56**, 21 (2015).
- ⁷³ O. Matsuda and O.B. Wright, *JOSA B* **19**, 3028 (2002).
- ⁷⁴ A. Rodriguez, A. Rodriguez, P. Priya, P. Priya, O. Ortiz, P. Senellart, C. Gomez-Carbonell, A. Lemaître, M. Esmann, M. Esmann, N.D. Lanzillotti-Kimura, and N.D. Lanzillotti-Kimura, *Opt. Express* **29**, 2637 (2021).
- ⁷⁵ O. Ortiz, F. Pastier, A. Rodriguez, Priya, A. Lemaitre, C. Gomez-Carbonell, I. Sagnes, A. Harouri, P. Senellart, V. Giesz, M. Esmann, and N.D. Lanzillotti-Kimura, *Appl. Phys. Lett.* **117**, 183102 (2020).
- ⁷⁶ N.D. Lanzillotti-Kimura, A. Fainstein, B. Perrin, B. Jusserand, O. Mauguin, L. Largeau, and A. Lemaître, *Phys. Rev. Lett.* **104**, 197402 (2010).
- ⁷⁷ S. Mookherjea and A. Yariv, *IEEE J. Sel. Top. Quantum Electron.* **8**, 448 (2002).
- ⁷⁸ J.K. Poon, L. Zhu, G.A. DeRose, and A. Yariv, *Opt. Lett.* **31**, 456 (2006).
- ⁷⁹ A. Yariv, Y. Xu, R.K. Lee, and A. Scherer, *Opt. Lett.* **24**, 711 (1999).
- ⁸⁰ R. Sapienza, P. Costantino, D. Wiersma, M. Ghulinyan, C.J. Oton, and L. Pavesi, *Phys. Rev. Lett.* **91**, 263902 (2003).
- ⁸¹ A.E. Bruchhausen, N.D. Lanzillotti-Kimura, B. Jusserand, A. Soukiassian, L. Xie, X.Q. Pan, T. Dekorsy, D.G. Schlom, and A. Fainstein, *Phys. Rev. Mater.* **2**, 106002 (2018).
- ⁸² N.D. Lanzillotti-Kimura, A. Fainstein, B. Jusserand, and A. Lemaître, *AIP Conf. Proc.* **1199**, 223 (2010).
- ⁸³ N.D. Lanzillotti Kimura, A. Fainstein, and B. Jusserand, *Phys. Rev. B* **71**, 041305 (2005).
- ⁸⁴ F. Bloch, *Z Phys* **52**, 555 (1928).
- ⁸⁵ C. Zener, *Proc R Soc Lond.* **A145**, 523 (1934).
- ⁸⁶ C. Waschke, H.G. Roskos, R. Schwedler, K. Leo, H. Kurz, and K. Köhler, *Phys. Rev. Lett.* **70**, 3319 (1993).
- ⁸⁷ J. Feldmann, K. Leo, J. Shah, D.A.B. Miller, J.E. Cunningham, T. Meier, G. von Plessen, A. Schulze, P. Thomas, and S. Schmitt-Rink, *Phys. Rev. B* **46**, 7252 (1992).
- ⁸⁸ C.L. Kane and E.J. Mele, *Phys. Rev. Lett.* **95**, 226801 (2005).
- ⁸⁹ Y. Zhang, Y.-W. Tan, H.L. Stormer, and P. Kim, *Nature* **438**, 201 (2005).
- ⁹⁰ B.A. Bernevig, T.L. Hughes, and S.-C. Zhang, *Science* **314**, 1757 (2006).
- ⁹¹ D.J. Thouless, M. Kohmoto, M.P. Nightingale, and M. den Nijs, *Phys. Rev. Lett.* **49**, 405 (1982).
- ⁹² W.P. Su, J.R. Schrieffer, and A.J. Heeger, *Phys. Rev. Lett.* **42**, 1698 (1979).
- ⁹³ A.J. Heeger, *Rev. Mod. Phys.* **73**, 681 (2001).
- ⁹⁴ F.D.M. Haldane and S. Raghu, *Phys. Rev. Lett.* **100**, 013904 (2008).
- ⁹⁵ M. Hafezi, E.A. Demler, M.D. Lukin, and J.M. Taylor, *Nat. Phys.* **7**, 907 (2011).
- ⁹⁶ J. Zak, *Phys. Rev. Lett.* **62**, 2747 (1989).
- ⁹⁷ M.V. Berry and F.R. S, *Proc R Soc Lond A* **392**, 45 (1984).
- ⁹⁸ M. Xiao, G. Ma, Z. Yang, P. Sheng, Z.Q. Zhang, and C.T. Chan, *Nat. Phys.* **11**, 240 (2015).
- ⁹⁹ M. Xiao, Z.Q. Zhang, and C.T. Chan, *Phys. Rev. X* **4**, 021017 (2014).
- ¹⁰⁰ A. Amo, A. Lemaître, E. Galopin, I. Sagnes, J. Bloch, L.L. Gratiet, P. St-Jean, T. Ozawa, and V. Goblot, *Nat. Photonics* **11**, 651 (2017).
- ¹⁰¹ M. Atala, M. Aidelsburger, J.T. Barreiro, D. Abanin, T. Kitagawa, E. Demler, and I. Bloch, *Nat. Phys.* **9**, 795 (2013).
- ¹⁰² Y. Guo, T. Dekorsy, and M. Hettich, *Sci. Rep.* **7**, 18043 (2017).
- ¹⁰³ C. Brendel, V. Peano, O. Painter, and F. Marquardt, *Phys. Rev. B* **97**, 020102 (2018).
- ¹⁰⁴ D.B. Sohn, S. Kim, and G. Bahl, *Nat. Photonics* **12**, 91 (2018).
- ¹⁰⁵ V. Peano, C. Brendel, M. Schmidt, and F. Marquardt, *Phys. Rev. X* **5**, 031011 (2015).
- ¹⁰⁶ X. Zhu, H. Ramezani, C. Shi, J. Zhu, and X. Zhang, *Phys. Rev. X* **4**, 031042 (2014).
- ¹⁰⁷ A. Fainstein and B. Jusserand, *Phys. Rev. B* **57**, 2402 (1998).
- ¹⁰⁸ B. Jusserand, F. Alexandre, J. Dubard, and D. Paquet, *Phys. Rev. B* **33**, 2897 (1986).
- ¹⁰⁹ P. Santos, M. Hundhausen, and L. Ley, *Phys. Rev. B* **33**, 1516 (1986).

- ¹¹⁰ G. Arregui, O. Ortíz, M. Esmann, C.M. Sotomayor-Torres, C. Gomez-Carbonell, O. Mauguin, B. Perrin, A. Lemaître, P.D. García, and N.D. Lanzillotti-Kimura, *APL Photonics* **4**, 030805 (2019).
- ¹¹¹ W.P. Su, J.R. Schrieffer, and A.J. Heeger, *Phys. Rev. Lett.* **42**, 1698 (1979).
- ¹¹² W.P. Su, J.R. Schrieffer, and A.J. Heeger, *Phys. Rev. B* **22**, 2099 (1980).
- ¹¹³ R. Jackiw and C. Rebbi, *Phys. Rev. D* **13**, 3398 (1976).
- ¹¹⁴ A.J. Heeger, S. Kivelson, J.R. Schrieffer, and W.-P. Su, *Rev. Mod. Phys.* **60**, 781 (1988).
- ¹¹⁵ M. Esmann, F.R. Lamberti, A. Lemaître, and N.D. Lanzillotti-Kimura, *Phys. Rev. B* **98**, 161109 (2018).
- ¹¹⁶ A. Naik, O. Buu, M.D. LaHaye, A.D. Armour, A.A. Clerk, M.P. Blencowe, and K.C. Schwab, *Nature* **443**, 193 (2006).
- ¹¹⁷ J. Chan, T.P.M. Alegre, A.H. Safavi-Naeini, J.T. Hill, A. Krause, S. Gröblacher, M. Aspelmeyer, and O. Painter, *Nature* **478**, 89 (2011).
- ¹¹⁸ U. Delić, M. Reisenbauer, K. Dare, D. Grass, V. Vuletić, N. Kiesel, and M. Aspelmeyer, *Science* **367**, 892 (2020).
- ¹¹⁹ S. Gigan, H.R. Böhm, M. Paternostro, F. Blaser, G. Langer, J.B. Hertzberg, K.C. Schwab, D. Bäuerle, M. Aspelmeyer, and A. Zeilinger, *Nature* **444**, 67 (2006).
- ¹²⁰ S. Gröblacher, K. Hammerer, M.R. Vanner, and M. Aspelmeyer, *Nature* **460**, 724 (2009).
- ¹²¹ D. Windey, C. Gonzalez-Ballester, P. Maurer, L. Novotny, O. Romero-Isart, and R. Reimann, *Phys. Rev. Lett.* **122**, 123601 (2019).
- ¹²² F. Tebbenjohanns, M. Frimmer, V. Jain, D. Windey, and L. Novotny, *Phys. Rev. Lett.* **124**, 013603 (2020).
- ¹²³ C.Y.T. Huang, F. Kargar, T. Debnath, B. Debnath, M.D. Valentin, R. Synowicki, S. Schoeche, R.K. Lake, and A.A. Balandin, *Nanotechnology* **31**, 30LT01 (2020).
- ¹²⁴ A. Fainstein, N.D. Lanzillotti-Kimura, B. Jusserand, and B. Perrin, *Phys. Rev. Lett.* **110**, 037403 (2013).
- ¹²⁵ N.D. Lanzillotti-Kimura, A. Fainstein, and B. Jusserand, *Ultrasonics* **56**, 80 (2015).
- ¹²⁶ O. Matsuda, T. Tachizaki, T. Fukui, J.J. Baumberg, and O.B. Wright, *Phys. Rev. B* **71**, 115330 (2005).
- ¹²⁷ M.F. Pascual Winter, G. Rozas, A. Fainstein, B. Jusserand, B. Perrin, A. Huynh, P.O. Vaccaro, and S. Saravanan, *Phys. Rev. Lett.* **98**, 265501 (2007).
- ¹²⁸ V. Villafañe, P. Soubelet, A.E. Bruchhausen, N.D. Lanzillotti-Kimura, B. Jusserand, A. Lemaître, and A. Fainstein, *Phys. Rev. B* **94**, 205308 (2016).
- ¹²⁹ S. Anguiano, P. Sesin, A.E. Bruchhausen, F.R. Lamberti, I. Favero, M. Esmann, I. Sagnes, A. Lemaître, N.D. Lanzillotti-Kimura, P. Senellart, and A. Fainstein, *Phys. Rev. A* **98**, 063810 (2018).
- ¹³⁰ S. Anguiano, A.E. Bruchhausen, I. Favero, I. Sagnes, A. Lemaître, N.D. Lanzillotti-Kimura, and A. Fainstein, *Phys. Rev. A* **98**, 013816 (2018).
- ¹³¹ J. Restrepo, C. Ciuti, and I. Favero, *Phys. Rev. Lett.* **112**, 013601 (2014).
- ¹³² J.C.G. Henriques, T.G. Rappoport, Y.V. Bludov, M.I. Vasilevskiy, and N.M.R. Peres, *Phys. Rev. A* **101**, 043811 (2020).
- ¹³³ M. Xiao, G. Ma, Z. Yang, P. Sheng, Z.Q. Zhang, and C.T. Chan, *Nat. Phys.* **11**, 240 (2015).
- ¹³⁴ T. Ozawa, H.M. Price, A. Amo, N. Goldman, M. Hafezi, L. Lu, M.C. Rechtsman, D. Schuster, J. Simon, O. Zilberberg, and I. Carusotto, *Rev. Mod. Phys.* **91**, 015006 (2019).
- ¹³⁵ M. Hafezi, S. Mittal, J. Fan, A. Migdall, and J.M. Taylor, *Nat. Photonics* **7**, 1001 (2013).
- ¹³⁶ M. Hafezi, E.A. Demler, M.D. Lukin, and J.M. Taylor, *Nat. Phys.* **7**, 907 (2011).
- ¹³⁷ L. Lu, J.D. Joannopoulos, and M. Soljačić, *Nat. Photonics* **8**, 821 (2014).
- ¹³⁸ P.A. Kalozoumis, G. Theocharis, V. Achilleos, S. Félix, O. Richoux, and V. Pagneux, *Phys. Rev. A* **98**, 023838 (2018).
- ¹³⁹ L.M. Nash, D. Kleckner, A. Read, V. Vitelli, A.M. Turner, and W.T.M. Irvine, *Proc. Natl. Acad. Sci.* **112**, 14495 (2015).
- ¹⁴⁰ S. Klembt, T.H. Harder, O.A. Egorov, K. Winkler, R. Ge, M.A. Bandres, M. Emmerling, L. Worschech, T.C.H. Liew, M. Segev, C. Schneider, and S. Höfling, *Nature* **562**, 552 (2018).
- ¹⁴¹ M. Milicevic, G. Montambaux, T. Ozawa, O. Jamadi, B. Real, I. Sagnes, A. Lemaître, L. Le Gratiet, A. Harouri, J. Bloch, and A. Amo, *Phys Rev X* **9**, 031010 (2019).
- ¹⁴² Y. Meng, X. Wu, R.-Y. Zhang, X. Li, P. Hu, L. Ge, Y. Huang, H. Xiang, D. Han, S. Wang, and W. Wen, *New J. Phys.* **20**, 073032 (2018).
- ¹⁴³ J. Yin, M. Ruzzene, J. Wen, D. Yu, L. Cai, and L. Yue, *Sci. Rep.* **8**, 1 (2018).

- ¹⁴⁴ X. Li, Y. Meng, X. Wu, S. Yan, Y. Huang, S. Wang, and W. Wen, *Appl. Phys. Lett.* **113**, 203501 (2018).
- ¹⁴⁵ Z. Wang, D. Zhao, J. Luo, R. Wang, and H. Yang, *Appl. Phys. Lett.* **116**, 013102 (2020).
- ¹⁴⁶ M. Xiao, Z.Q. Zhang, and C.T. Chan, *Phys. Rev. X* **4**, 021017 (2014).
- ¹⁴⁷ L.-Y. Zheng, V. Achilleos, O. Richoux, G. Theocharis, and V. Pagneux, *Phys. Rev. Appl.* **12**, 034014 (2019).
- ¹⁴⁸ O. Ortiz, P. Priya, A. Rodriguez, A. Lemaître, M. Esmann, and N.D. Lanzillotti-Kimura, *ArXiv* 200714753 (2020).
- ¹⁴⁹ P.W. Anderson, *Phys. Rev.* **109**, 1492 (1958).
- ¹⁵⁰ F. Evers and A.D. Mirlin, *Rev. Mod. Phys.* **80**, 1355 (2008).
- ¹⁵¹ J. Jäckle, *Solid State Commun.* **39**, 1261 (1981).
- ¹⁵² P.-E. Wolf and G. Maret, *Phys. Rev. Lett.* **55**, 2696 (1985).
- ¹⁵³ M.P.V. Albada and A. Lagendijk, *Phys. Rev. Lett.* **55**, 2692 (1985).
- ¹⁵⁴ S. John, *Phys. Rev. Lett.* **58**, 2486 (1987).
- ¹⁵⁵ G. Arregui, N.D. Lanzillotti-Kimura, C.M. Sotomayor-Torres, and P.D. García, *Phys. Rev. Lett.* **122**, 043903 (2019).
- ¹⁵⁶ R. Kuszelewicz, I. Ganne, I. Sagnes, G. Sleky, and M. Brambilla, *Phys. Rev. Lett.* **84**, 6006 (2000).
- ¹⁵⁷ T. Rivera, F.R. Ladan, A. Izraël, R. Azoulay, R. Kuszelewicz, and J.L. Oudar, *Appl. Phys. Lett.* **64**, 869 (1994).
- ¹⁵⁸ V.B. Taranenko, I. Ganne, R.J. Kuszelewicz, and C.O. Weiss, *Phys. Rev. A* **61**, 063818 (2000).
- ¹⁵⁹ T. Jacqmin, I. Carusotto, I. Sagnes, M. Abbarchi, D.D. Solnyshkov, G. Malpuech, E. Galopin, A. Lemaître, J. Bloch, and A. Amo, *Phys. Rev. Lett.* **112**, 116402 (2014).
- ¹⁶⁰ M. Galbiati, L. Ferrier, D.D. Solnyshkov, D. Tanese, E. Wertz, A. Amo, M. Abbarchi, P. Senellart, I. Sagnes, A. Lemaître, E. Galopin, G. Malpuech, and J. Bloch, *Phys. Rev. Lett.* **108**, 126403 (2012).
- ¹⁶¹ H.S. Nguyen, D. Gerace, I. Carusotto, D. Sanvitto, E. Galopin, A. Lemaître, I. Sagnes, J. Bloch, and A. Amo, *Phys. Rev. Lett.* **114**, 036402 (2015).
- ¹⁶² V. Giesz, N. Somaschi, G. Hornecker, T. Grange, B. Reznichenko, L. De Santis, J. Demory, C. Gomez, I. Sagnes, A. Lemaître, O. Krebs, N.D. Lanzillotti-Kimura, L. Lanco, A. Auffeves, and P. Senellart, *Nat. Commun.* **7**, 11986 (2016).
- ¹⁶³ S.A. Maier, *Plasmonics: Fundamentals and Applications*, 2007 edition (Springer, New York, 2007).
- ¹⁶⁴ S. Mazzucco, N. Geuquet, J. Ye, O. Stéphan, W. Van Roy, P. Van Dorpe, L. Henrard, and M. Kociak, *Nano Lett.* **12**, 1288 (2012).
- ¹⁶⁵ S. Mazzucco, O. Stéphan, C. Colliex, I. Pastoriza-Santos, L.M. Liz-Marzan, J.G. de Abajo, and M. Kociak, *Eur. Phys. J. - Appl. Phys.* **54**, (2011).
- ¹⁶⁶ J. Nelayah, M. Kociak, O. Stéphan, F.J. García de Abajo, M. Tencé, L. Henrard, D. Taverna, I. Pastoriza-Santos, L.M. Liz-Marzán, and C. Colliex, *Nat. Phys.* **3**, 348 (2007).
- ¹⁶⁷ V.J. Sorger, N.D. Lanzillotti-Kimura, R.-M. Ma, and X. Zhang, *Nanophotonics* **1**, 17 (2012).
- ¹⁶⁸ C. Symonds, G. Lheureux, J.P. Hugonin, J.J. Greffet, J. Laverdant, G. Brucoli, A. Lemaître, P. Senellart, and J. Bellessa, *Nano Lett.* **13**, 3179 (2013).
- ¹⁶⁹ R.F. Oulton, V.J. Sorger, T. Zentgraf, R.-M. Ma, C. Gladden, L. Dai, G. Bartal, and X. Zhang, *Nature* **461**, 629 (2009).
- ¹⁷⁰ G. Zheng, H. Mühlenbernd, M. Kenney, G. Li, T. Zentgraf, and S. Zhang, *Nat. Nanotechnol.* **10**, 308 (2015).
- ¹⁷¹ P. Bharadwaj, B. Deutsch, and L. Novotny, *Adv. Opt. Photonics* **1**, 438 (2009).
- ¹⁷² L. Novotny and N. van Hulst, *Nat. Photonics* **5**, 83 (2011).
- ¹⁷³ L. Novotny, *Phys. Rev. Lett.* **98**, 266802 (2007).
- ¹⁷⁴ N.D. Lanzillotti-Kimura, K.P. O'Brien, J. Rho, H. Suchowski, X. Yin, and X. Zhang, *Phys. Rev. B* **97**, 235403 (2018).
- ¹⁷⁵ Y. Imade, R. Ulbricht, M. Tomoda, O. Matsuda, G. Seniutinas, S. Juodkazis, and O.B. Wright, *Nano Lett.* **17**, 6684 (2017).
- ¹⁷⁶ R. Berte, F. Della Picca, M. Poblet, Y. Li, E. Cortés, R.V. Craster, S.A. Maier, and A.V. Bragas, *Phys. Rev. Lett.* **121**, 253902 (2018).
- ¹⁷⁷ C. Yi, P.D. Dongare, M.-N. Su, W. Wang, D. Chakraborty, F. Wen, W.-S. Chang, J.E. Sader, P. Nordlander, N.J. Halas, and S. Link, *Proc. Natl. Acad. Sci.* **114**, 11621 (2017).
- ¹⁷⁸ B. Gayral, J.M. Gérard, B. Legrand, E. Costard, and V. Thierry-Mieg, *Appl. Phys. Lett.* **72**, 1421 (1998).

- ¹⁷⁹ F.R. Lamberti, Q. Yao, L. Lanco, D.T. Nguyen, M. Esmann, A. Fainstein, P. Sesin, S. Anguiano, V. Villafañe, A. Bruchhausen, P. Senellart, I. Favero, and N.D. Lanzillotti-Kimura, *Opt. Express* **25**, 24437 (2017).
- ¹⁸⁰ S. Anguiano, A.E. Bruchhausen, B. Jusserand, I. Favero, F.R. Lamberti, L. Lanco, I. Sagnes, A. Lemaître, N.D. Lanzillotti-Kimura, P. Senellart, and A. Fainstein, *Phys. Rev. Lett.* **118**, 263901 (2017).
- ¹⁸¹ J. Restrepo, I. Favero, and C. Ciuti, *Phys. Rev. A* **95**, 023832 (2017).
- ¹⁸² M. Esmann, F.R. Lamberti, A. Harouri, L. Lanco, I. Sagnes, I. Favero, G. Aubin, C. Gomez-Carbonell, A. Lemaître, O. Krebs, P. Senellart, and N.D. Lanzillotti-Kimura, *Optica* **6**, 854 (2019).
- ¹⁸³ A. Bartels, R. Cerna, C. Kistner, A. Thoma, F. Hudert, C. Janke, and T. Dekorsy, *Rev. Sci. Instrum.* **78**, 035107 (2007).
- ¹⁸⁴ D. Cadeddu, J. Teissier, F.R. Braakman, N. Gregersen, P. Stepanov, J.-M. Gérard, J. Claudon, R.J. Warburton, M. Poggio, and M. Munsch, *Appl. Phys. Lett.* **108**, 011112 (2016).
- ¹⁸⁵ F. Haupt, S.S.R. Oemrawsingh, S.M. Thon, H. Kim, D. Kleckner, D. Ding, D.J. Suntrup, P.M. Petroff, and D. Bouwmeester, *Appl. Phys. Lett.* **97**, 131113 (2010).
- ¹⁸⁶ A. Schlehahn, S. Fischbach, R. Schmidt, A. Kaganskiy, A. Strittmatter, S. Rodt, T. Heindel, and S. Reitzenstein, *Sci. Rep.* **8**, 1 (2018).
- ¹⁸⁷ H. Snijders, J.A. Frey, J. Norman, V.P. Post, A.C. Gossard, J.E. Bowers, M.P. van Exter, W. Löffler, and D. Bouwmeester, *Phys. Rev. Appl.* **9**, 031002 (2018).
- ¹⁸⁸ T. Ellenbogen, K. Seo, and K.B. Crozier, *Nano Lett.* **12**, 1026 (2012).
- ¹⁸⁹ O. Ortíz, M. Esmann, and N.D. Lanzillotti-Kimura, *Phys. Rev. B* **100**, 085430 (2019).
- ¹⁹⁰ R.P. Beardsley, A.V. Akimov, M. Henini, and A.J. Kent, *Phys. Rev. Lett.* **104**, 085501 (2010).
- ¹⁹¹ A.V. Akimov, A.V. Scherbakov, D.R. Yakovlev, C.T. Foxon, and M. Bayer, *Phys. Rev. Lett.* **97**, 037401 (2006).
- ¹⁹² B.J. Eggleton, P.S. Westbrook, R.S. Windeler, S. Spälter, and T.A. Strasser, *Opt. Lett.* **24**, 1460 (1999).
- ¹⁹³ A. Godet, A. Ndao, T. Sylvestre, V. Pecheur, S. Lebrun, G. Pauliat, J.-C. Beugnot, and K.P. Huy, *Optica* **4**, 1232 (2017).
- ¹⁹⁴ M. Merklein, B. Stiller, K. Vu, S.J. Madden, and B.J. Eggleton, *Nat. Commun.* **8**, 1 (2017).
- ¹⁹⁵ Y. Stern, K. Zhong, T. Schneider, R. Zhang, Y. Ben-Ezra, M. Tur, and A. Zadok, *Photonics Res.* **2**, B18 (2014).
- ¹⁹⁶ R. Pant, C.G. Poulton, D.-Y. Choi, H. Mcfarlane, S. Hile, E. Li, L. Thevenaz, B. Luther-Davies, S.J. Madden, and B.J. Eggleton, *Opt. Express* **19**, 8285 (2011).
- ¹⁹⁷ R.P. Beardsley, A.V. Akimov, M. Henini, and A.J. Kent, *Phys. Rev. Lett.* **104**, 085501 (2010).
- ¹⁹⁸ T. Czerniuk, J. Tepper, A.V. Akimov, S. Unsleber, C. Schneider, M. Kamp, S. Höfling, D.R. Yakovlev, and M. Bayer, *Appl. Phys. Lett.* **106**, 041103 (2015).
- ¹⁹⁹ C.-K. Sun, J.-C. Liang, and X.-Y. Yu, *Phys. Rev. Lett.* **84**, 179 (2000).
- ²⁰⁰ D. Schneider, F. Liaqat, E.H. El Boudouti, Y. El Hassouani, B. Djafari-Rouhani, W. Tremel, H.-J. Butt, and G. Fytas, *Nano Lett.* **12**, 3101 (2012).
- ²⁰¹ F. Huang, X. Zhang, and B.Z. Tang, *Mater. Chem. Front.* **3**, 10 (2018).
- ²⁰² P. Innocenzi and L. Malfatti, *Chem. Soc. Rev.* **42**, 4198 (2013).
- ²⁰³ R.M. Gazoni, M.G. Bellino, M.C. Fuertes, G. Giménez, G.J.A.A. Soler-Illia, and M.L.M. Ricci, *J. Mater. Chem. C* **5**, 3445 (2017).
- ²⁰⁴ G.J.A.A. Soler-Illia and O. Azzaroni, *Chem. Soc. Rev.* **40**, 1107 (2011).
- ²⁰⁵ M.J. Penelas, C.B. Contreras, P.C. Angelomé, A. Wolosiuk, O. Azzaroni, and G.J.A.A. Soler-Illia, [10.26434/Chemrxiv.8313788.v1](https://doi.org/10.26434/chemrxiv.8313788.v1) (2019).
- ²⁰⁶ T. Paik, S.-H. Hong, E.A. Gaulding, H. Caglayan, T.R. Gordon, N. Engheta, C.R. Kagan, and C.B. Murray, *ACS Nano* **8**, 797 (2014).
- ²⁰⁷ A. Leitis, A. Heßler, S. Wahl, M. Wuttig, T. Taubner, A. Tittel, and H. Altug, *Adv. Funct. Mater.* **30**, 1910259 (2020).
- ²⁰⁸ Z.L. Sámson, K.F. MacDonald, F. De Angelis, B. Gholipour, K. Knight, C.C. Huang, E. Di Fabrizio, D.W. Hewak, and N.I. Zheludev, *Appl. Phys. Lett.* **96**, 143105 (2010).
- ²⁰⁹ C.U. Hail, A.-K.U. Michel, D. Poulidakos, and H. Eghlidi, *Adv. Opt. Mater.* **7**, 1801786 (2019).
- ²¹⁰ I. Hamberg and C.G. Granqvist, *J. Appl. Phys.* **60**, R123 (1986).
- ²¹¹ E. Feigenbaum, K. Diest, and H.A. Atwater, *Nano Lett.* **10**, 2111 (2010).
- ²¹² C. Galland, N. Sangouard, N. Piro, N. Gisin, and T.J. Kippenberg, *Phys. Rev. Lett.* **112**, 143602 (2014).

- ²¹³ M.D. Anderson, S. Tarrago Velez, K. Seibold, H. Flayac, V. Savona, N. Sangouard, and C. Galland, *Phys. Rev. Lett.* **120**, 233601 (2018).
- ²¹⁴ S.T. Velez, K. Seibold, N. Kipfer, M.D. Anderson, V. Sudhir, and C. Galland, *Phys. Rev. X* **9**, 041007 (2019).
- ²¹⁵ F.S. de A. Júnior, A. Saraiva, M.F. Santos, B. Koiller, R. de M. e Souza, A.P. Pena, R.A. Silva, C.H. Monken, and A. Jorio, *Phys. Rev. B* **99**, 100503 (2019).
- ²¹⁶ A. Saraiva, F.S. de A. Júnior, R. de Melo e Souza, A.P. Pena, C.H. Monken, M.F. Santos, B. Koiller, and A. Jorio, *Phys. Rev. Lett.* **119**, 193603 (2017).

Acknowledgments

It has been a long way since I decided to study phonons. I was fortunate to have great mentors throughout my scientific career that inspired me and transferred the excitement of doing research: A. Fainstein, B. Perrin, B. Jusserand, X. Zhang, and P. Senellart. To them, my most profound recognition.

I want to thank to:

The people who worked by my side. Without their help, work, discussions, and a long et cetera, I could have never reached this point. To all the Ph.D. students, colleagues, and postdocs, particularly to A. Bruchhausen, G. Rozas, K. O'Brien, V. Villafañe, F. Lamberti, M. Esmann, O. Ortiz, A. Rodriguez, Priya, and E. Cardozo.

The researchers who were always there, just checking on me, ready to listen and discuss, and sometimes inspiring crazy new ideas. Thanks to those who, besides helluva collaborators, are my friends. Special thanks to Bernard Perrin, Clivia Sotomayor-Torres, David García, Pascale Senellart, Loic Lanco, Ivan Favero, Aristide Lemaitre, Isabelle Sagnes, Antonio García-Martin, and Galo Soler-Illia.

All my friends who shared just too much of the frustrations and unfruitful experiments and never had enough recognition in the (few) moments of glory. To my family.

The C2N, the CNRS, and the ERC, who let me make my dreams come true.